High-Turbidity Bottom Mixed-Layer Water on the Shelf off Hokkaido in the Okhotsk Sea: Distribution, Seasonal Variations, and Spreading

Tomohiro Nakamura[1], Junki Ueda[2+], Tokihiro Kono[3], Jun Nishioka[1], Humio Mitsudera[1], Kaoru Ito[1*]

1 Pan-Okhotsk Research Center, Institute of Low Temperature Science, Hokkaido University, Sapporo, 060-0819, Japan
2 Graduate School of Environmental Science, Hokkaido University, Sapporo, 060-0810, Japan
3 Coastal Research Engineering Co., Ltd., Sapporo, 060-0009, Japan

\+ Now at Japan Weather Association, Tokyo, 170-6055, Japan
* Now at Atmosphere and Ocean Research Institute, the University of Tokyo, Chiba, 277-8564, Japan

Corresponding author: Tomohiro Nakamura, nakamura@lowtem.hokudai.ac.jp, Tel:+81-11-706-7494, Fax (office representative): +81-11-706-7142, ORCID: 0000-0001-7632-2733

Abstract

The Okhotsk Sea coast of Hokkaido and the Kuril Basin exhibit high primary production, supported by nutrient supply through material circulation. As part of this circulation, we focused on high turbidity water in the bottom mixed layer (BML) on the shelf off Hokkaido and its spreading. Our observations in spring and autumn showed a thick, high-turbidity BML across the shelf, originating mostly from the Soya Strait and flowing toward the Shiretoko Peninsula and into the Kuril Basin. Analysis of past observation data and an ocean model output revealed that the thick BML was present year-round, suggesting the continuous supply of high-turbidity waters. BML thickness and density were highest in spring and lowest in winter and peaked offshore of the Soya Warm Current. Using the model output, we conducted Lagrangian tracking of BML water. BML waters with low density mostly flowed into the North Pacific quickly through shallow straits near Hokkaido, whereas higher-density BML waters spread into the Kuril Basin, remaining there longer before eventually flowing into the North Pacific through deep straits. We also showed seasonal variations primarily driven by density variations, interannual changes associated with flow field variation, and sensitivity to sinking rates for sinking particles. The results suggest that high-turbidity bottom waters off Hokkaido in the Okhotsk Sea are transported to the Kuril Basin and North Pacific, potentially impacting material circulation and ecosystems. In particular, high-turbidity waters lighter than 26.7 σ_θ may be entrained into the euphotic zone by winter mixing, contributing to the next spring bloom.

Keywords: High-turbidity water in bottom mixed layer, Hokkaido shelf in the Okhotsk Sea, Material circulation, Lagrangian tracking, Identification of Soya Strait origin waters

Statements and Declarations

As far as we are aware, there are no conflicts of interest to declare.

1. Introduction

The Okhotsk Sea shelf off Hokkaido, extending to the Kuril Basin (Fig. 1a), boasts high primary production (Mustapha et al. 2009; Kasai et al. 2010; Kudo et al. 2011; Kishi et al. 2021), supporting high biodiversity and productive fisheries. This high primary production requires a supply of nutrients. However, the mechanisms of nutrient cycling in this area remain only partially understood. Previously identified nutrient supply processes and sources include the mixing of Soya Warm Current Water (SWCW) and subsurface cold water (also called intermediate cold water or dichothermal water), winter mixing, sea ice, and the East Sakhalin Current Water (Kasai et al. 2010; Kudo et al. 2011; Kanna et al. 2018; Kishi et al. 2021). As another potential contributor to material circulation in this area, this study focuses on high-turbidity water in the bottom mixed layer (BML) on the Hokkaido shelf, which has not received attention from this viewpoint.

In summer (August), high-turbidity water in the thick BML has been observed on the Hokkaido shelf, particularly offshore of the Soya Warm Current (SWC, Wadaka 2008; Wadaka et al. 2009). The development of the BML leads to the resuspension of bottom sediments, thus increasing turbidity. Marine geological and geophysical observations indicated that as swift bottom currents around the Soya Strait slows downstream, the seafloor transitions from erosional rocky zones to gravel-covered areas and then to coarse to very fine sand deposition areas along the coast, approximately 30–40 km from the shore (Ikehara et al. 2001b). These sand areas indeed exhibit ripples and current lineations, suggesting relatively fast bottom currents, oriented northwest-southeast (Ikehara et al. 2001a). Muddy sediments (silt and silty clay) are distributed offshore of the sand areas, forming high-turbidity water near the bottom (Noda et al. 2001; 2002a; b; Ikehara et al. 2001a; b; Katayama et al. 2002; Tanabe and Sakamoto 2002).

The high-turbidity water on the Hokkaido shelf contains nutrients. Suspended particles in the high-turbidity water include both organic matter from phytoplankton detritus and mineral components from silt in bottom sediments (Wadaka 2008). High concentrations of iron have also been observed in the high-turbidity water (Imai 2023).

It is reasonable to suppose that both the high-turbidity water and BML water flow from the shelf into the Kuril Basin and further into the North Pacific, particularly along the eastern Hokkaido coast, based on previous studies on the SWC or the East Sakhalin Current (ESC). In fact, the previous observations in August showed that the high-turbidity water flows along the coast with the SWC, detaches from the shelf off Abashiri (Fig. 1b), and continues along the western coast of the Shiretoko Peninsula (Wadaka 2008; Wadaka et al. 2009). The SWC dominates from April to November, while the ESC prevails from November to April (e.g., Itoh and Ohshima 2000). The SWC enters the Okhotsk Sea through the Soya Strait, flows along the Hokkaido coast, and detaches from the coast at the Shiretoko Peninsula, entering the Kuril Basin (Aota 1975; Takizawa 1982; Matsuyama et al. 2006; Ebuchi et al. 2006; Fukamachi et al. 2008;

Ohshima et al. 2017). Offshore of the SWC, the Cold Water Belt appears from spring to autumn (Danchenkov et al. 1999; Ishizu et al. 2006; 2008) and transports the Japan Sea Intermediate Water (Mitsudera et al. 2011; Kuma et al. 2014; Iida et al. 2018; Chiba et al. 2021). The ESC flows southward from the east of Sakhalin to Hokkaido during winter (Itoh and Ohshima 2000; Ohshima et al. 2002; Mizuta et al. 2003; Ebuchi 2006). Both the SWC and the ESC either directly flow into the Pacific or spread across the Kuril Basin (Takizawa 1982; Wakatsuchi and Martin 1991; Mensah et al. 2019). The former inflowing water enters the Hokkaido Pacific shelf, forming the Coastal Oyashio Water, contributing to the primary production along the eastern Hokkaido coast and the Oyashio region (Nakamura et al. 2003; Kono and Sato 2010; Kuroda et al. 2019). The latter Kuril Basin water also enters the Pacific through the Kuril straits (Kurashina et al. 1967; Nakamura and Awaji 2004; Katsumata et al. 2004; Ohshima et al. 2010), being exposed to tidal mixing (Nakamura et al. 2006). It then merges with the East Kamchatka Current Water to form the Oyashio Water, serving as a major source of the North Pacific Intermediate Water (Kono and Kawasaki 1997; Yasuda et al. 1997).

Although such high-turbidity water in the BML is located below the euphotic zone in summer, it can be entrained into the euphotic zone by winter mixing or tidal mixing in the Kuril Straits, potentially contributing to a spring bloom in the surface layer as well as affecting the benthic ecosystem. Indeed, winter mixing reaches 26.6–26.7 σ_θ in the southern Okhotsk Sea, forming subsurface cold water (Kitani 1973; Takizawa 1982; Miura et al. 2002; Uehara et al. 2012; Mensah et al. 2019). Tidal mixing in the Kuril Straits can mix water down to 27.5 σ_θ from the surface (Nakamura and Awaji 2004; Itoh et al. 2011; Yagi et al. 2014).

Therefore, high-turbidity water on the Hokkaido shelf in the Okhotsk Sea would contribute to nutrient circulation and primary production across the shelf, Kuril Basin, eastern Hokkaido coast, and North Pacific. This is similar to the Dense Shelf Water (DSW) formed in the northern Okhotsk Sea (Kitani 1973). High-turbidity water near the bottom in the northwestern shelf of the Okhotsk Sea also contains high concentrations of iron and sinks as part of the DSW, influencing the Okhotsk Sea's material circulation and ecosystem (Nakatsuka et al. 2004a; b). Although denser than shelf water off Hokkaido, part of the DSW is entrained into the euphotic zone by tidal mixing in the Kuril Straits, supplying nutrients to the surface Oyashio region and influencing primary production (Nishioka et al. 2013; Uchimoto et al. 2011; Nakanowatari et al. 2017). It also supplies dissolved and suspended materials to the North Pacific intermediate layer (e.g., Warner et al. 1996; Nishioka et al. 2023). We expect similar processes to occur for high-turbidity water on the Hokkaido shelf after it enters the Kuril Basin.

However, the horizontal distribution and seasonal variation of high-turbidity water and the BML, and where they go beyond the Shiretoko Peninsula, remain unclear. Observations of turbidity are scarce and mostly limited to summer. Border issues and sea ice make it difficult to observe beyond Shiretoko and in winter. In this study, we first examine high-turbidity water and the BML on the Hokkaido Okhotsk-Sea shelf in Section 3, based on observations in spring and autumn. Second, we analyze the BML's distribution, seasonal variation, and development factors in Section 4, using past observation data and the output of an ocean general circulation model (OGCM). Third, in Section 5, we explore the spreading of the BML water and its time scale, using it as a proxy for high-turbidity water, by Lagrangian tracking with the OGCM output.

2. Data and Method

2.1 Observations of High-Turbidity Water

To confirm the presence of high-turbidity water in seasons other than summer, we conducted hydrographic observations with turbidity measurements in late autumn and spring. Figure 1b shows the three transects used in this study: the EW line extending east-west from the Hokkaido coast to the Kuril Basin, the S line crossing the shelf slope from the Shiretoko Peninsula, and the NS line running north-south along the southwestern edge of the Kuril Basin (corresponding to HO-U and ES-M, HO-D, and NS lines in the cruise plans). These transects were conducted during the three cruises summarized in Table 1.

The hydrographic observations with seawater sampling were conducted to approximately 10 m above the bottom, using a conductivity-temperature-depth (CTD)-carousel multiple sampler system (SBE 911plus and SBE 32 water samplers, Sea Bird Electronics). The CTD was also equipped with sensors for dissolved oxygen (SBE 43), turbidity and fluorescence (Seapoint Sensors), and beam transmission (WET Labs C-Star). Nevertheless, beam transmission data were not used in this study, as they were qualitatively similar to turbidity data. Dissolved oxygen sensor values were calibrated against dissolved oxygen concentrations measured by the Winkler method. The latter measurement was taken in 5–12 layers from the surface to the bottom at 4–5 representative stations during each cruise.

2.2 Past Hydrographic Data

To investigate the year-round presence and horizontal distribution of the thick BML, we analyzed historical temperature and salinity data. The data were provided by the Hokkaido Research Organization (HRO) and the Japan Oceanographic Data Center (JODC). The analysis area focused on the shelf (shallower than 300 m) around Hokkaido (141.5° E–145° E, 43.5° N–46° N). The HRO data spanned from April to December 1989–2021, and the JODC data covered January to December 1960–2016. The number of observations per season was 2349 in spring (Apr–Jun), 2419 in summer (Jul–Sep), 1523 in autumn (Oct–Dec), and 105 in winter (Jan–Mar). The number was limited in winter, requiring caution, but was generally sufficient for climatological analysis in other seasons. Vertical data intervals were 5 or 10 m for HRO and 10.4 m on average (std = 12.8 m) for JODC, indicating sufficient vertical resolution.

Estimating BML thickness required depth data. Whenever possible, we used depth measurements taken during observations. In cases where depth data were unavailable (all JODC sites and 197 HRO sites, 5.6%) or when measured depth was less than the deepest layer observed (109 HRO sites, 3.1%), we estimated depth using digital bathymetric charts from the Japan Hydrographic Association (M7015, M7016) for sites shallower than 100 m and the ETOPO1 1 Arc-Minute Global Relief Model (NOAA National Geophysical Data Center, 2009) for sites deeper than 100 m.

2.3 Ocean Model Data

To examine the factors contributing to BML development (Section 4) and to conduct Lagrangian tracking (Section 5), we used the free-run output of the operational system for monitoring and forecasting the status of coastal and open-ocean waters around Japan (JPN System) developed by the Meteorological Research Institute (MRI) of the Japan Meteorological Agency (JMA). This system consists of a two-way nested ocean general circulation model and a data assimilation system (Hirose et al. 2019). There are three levels of domains: global, North Pacific, and Japan coastal models. For this study, we used the Japan coastal model. The ocean general circulation model is based on the MRI.COM version 4.5 (Tsujino et al. 2017; Sakamoto et al. 2019), which solves primitive equations in a vertically rescaled height coordinate system, called the z* coordinate, and includes a sea-ice model. Atmospheric forcing data is the Japanese 55-year Reanalysis (JRA-55, Kobayashi et al. 2015) based surface dataset for driving ocean-sea ice models (JRA55-do, Tsujino et al. 2018). River runoff data is from a sub-dataset of JRA55-do (Suzuki et al. 2018), calculated from JRA-55 precipitation data at 0.25° horizontal resolution with daily intervals. Tide generating forces for the eight major tidal constituents are given explicitly (Sakamoto et al. 2013).

The Japan coastal model covers a region from 117° E–160° E and 20° N–52° N, with a horizontal resolution of approximately 2 km (1/33° longitude and 1/50° latitude). Vertically, it has 60 layers, with a resolution from 2 m at the surface, 20 m at 200 m depth, and to 600 m at 6,300 m depth, employing partial cells at the deepest layer and allowing a minimum mean water depth of 8 m in the z* coordinate. The analysis period was from January 1, 2008, to December 31, 2017, with daily mean outputs.

The free run used the data assimilation to create the initial condition. Unlike the assimilation system, it used higher-resolution forcing around Japan for wind and atmospheric pressure (MSM reanalysis produced by JMA) and for river runoff (Urakawa et al. 2016); for details, see Sakamoto et al. (2019). The free run effectively reproduced the velocity fields and water mass structures (Appendix A). In fact, it exhibited better agreement with observations of the SWC east of Abashiri (Inoue 2021). Since our aim is to understand the basic characteristics rather than conditions on specific dates, we used the free-run, which adheres to the model's inherent dynamics.

2.4 Lagrangian Tracking Method

To investigate the spread of water in the BML, we conducted particle tracking (Section 5) using TRACMASS (version 7.0). TRACMASS is a Lagrangian trajectory code designed for oceanic and atmospheric applications (Aldama-Campino et al. 2020) and provides accurate Lagrangian tracking with mass conservation (Doos et al. 2013; 2017). In this study, Lagrangian tracking was performed using the velocity fields from the JPN System. Considering swift currents with maximum speed exceeding 1.5 m/s, the tracking timestep was set short enough (15 minutes) to ensure that no particles moved more than one grid cell (approximately 2 km) within each step.

In the main analyses (Sections 5.1, 5.2, and 5.4), particles were distributed and tracked in three dimensions. Initially, one particle was placed per grid cell from the bottom to the top of the BML on the shelf off Hokkaido (43.98–45.58°N, 141.97–144.39°E, shallower than 220 meters). The initial number of particles, dependent on the seasonally varying BML thickness, was 13,002 in August (Sections 5.1 and 5.4), reaching a maximum of 17,375 in May and a minimum of 10,625 in February (Section 5.2). The domain for tracking was 141.84°E–154°E and 42°N–50°N, with particles not returning once they exited the domain. In the interannual variation analysis (Section 5.3), particles were tracked along the 26.6 σ_θ isopycnal surface to reduce computation time. Initially, one particle was placed per horizontal grid cell within the BML on the shelf off Hokkaido. The initial number of particles averaged around 1,000 and depended on the area with the BML density of 26.6 σ_θ. The domain for tracking was slightly larger (141.19°E–160.06°E and 41.96°N–52.04°N).

3. High-Turbidity Water and Thick Bottom Mixed Layer

High-turbidity water in a thick BML has been reported on the shelf off the Okhotsk Sea near Hokkaido, but previous observations were limited to summer, as described in the introduction. Therefore, we conducted observations in late autumn and spring to confirm the presence of high-turbidity water and thick BML (Section 3.1) and attempted to identify major water masses associated with high-turbidity water focusing on Soya Strait origin waters (Section 3.2).

3.1 Distributions of High-Turbidity Waters and the Bottom Mixed Layer

Relatively high-turbidity waters and a relatively thick BML were observed in December, April, and May along the east-west transect (EW line) extending from the shelf to the basin (Fig. 2a, d, g). High turbidity (say, > 0.15-0.2) was found near the bottom on the shelf (and in horizontal intrusions from a sloping seabed, e.g., around 30 km from the coast in Fig. 2d, g). Since fluorescence was low at these depths, the high turbidity was due to resuspended sediments rather than phytoplankton. Near-surface high turbidity in April and May was attributed to a spring bloom of phytoplankton (indicated by high fluorescence, not shown). The BML, characterized by vertically uniform density, exceeded 50 m in thickness in some locations, as indicated by the first or second density contours from the bottom. The BML density varied seasonally: around 26.5 σ_θ in December and 26.6–27 σ_θ in April and May. Areas of high turbidity generally corresponded with the BML but extended slightly above it.

To identify water masses that contained these high-turbidity waters on the shelf, Fig. 2 (b, e, h) presents vertical sections of potential temperature and salinity. In all three months, high-salinity, relatively warm SWCW was observed near the coast, with temperature and salinity fronts offshore (Cold Water Belt or dense SWCW in April and May). High-turbidity waters were frequently found in these regions. Subsurface cold water below 0 °C (dichothermal water) was also observed in all three months. High turbidity was found even in the dichothermal water that was in contact with the bottom (near the shelf break in December 2020). The dichothermal water extended to 400 m depth and 26.75 σ_θ in April 2021, and to 26.7 σ_θ in May 2022, indicating that winter mixing affected densities of 26.7 σ_θ or higher.

Downstream of the shelf and the EW line, relatively high turbidity was observed along the S line (Fig. 3), where the SWC flowed along the steep western slope of Shiretoko after leaving the shelf. In both December and April, turbidity was relatively high over the slope and in areas with relatively high temperatures (Fig.3a-b, d-e), indicating the influence of the SWCW or dense SWCW (though in April 2021, phytoplankton dominated at depths shallower than 100 m, indicated by high fluorescence). Turbidity was particularly high in December 2020, likely because it was after a storm (Dec 16–20). The density of high-turbidity water was centered around 26.4–26.65 σ_θ in December and 26.8–27 σ_θ in April, corresponding to the densities of high-turbidity water and BML water on the shelf. These observations suggest that high-turbidity water in the BML on the shelf spreads off the shelf in both spring and late autumn, not just in August.

Examining the EW line outside the shelf (Fig. 2) and the NS line (Fig. 3g-h) reveals that relatively high-turbidity water appeared on density layers similar to those on the shelf. This density consistency suggests the spread of high-turbidity water from the shelf, as explained below. In the deep-water area of the EW line, relatively high turbidity was concentrated in the relatively warm, low-density modified SWCW at around 26.6 σ_θ in December and extended from 26.6 to 27.0 σ_θ in April and May. On the NS line, higher turbidity in the south suggests that relatively high-turbidity waters moved northward after exiting the shelf near the Abashiri submarine canyon, rather than directly spreading eastward from the shelf. Although relatively high-turbidity water on the NS line had densities of 26.8–27 σ_θ, similar to those of the DSW, its higher temperature compared to the surrounding water and the increased turbidity to the south suggest that its origin was the dense SWCW from the Hokkaido shelf, rather than the DSW from the northern Okhotsk Sea.

These data suggest that much of the high-turbidity water originates from or is influenced by the SWCW. In the next section, we will examine the relationship between high-turbidity water and the SWCW and its variants.

3.2 High-Turbidity Waters and Soya Strait Origin Waters

To investigate the relationship between high-turbidity waters and the SWCW and its variants, we considered a method for identifying waters originating from the Soya Strait. For simplicity, we refer to relatively warm, high-salinity water masses originating from the Japan Sea via the Soya Strait—including the SWCW, Cold Water Belt, Forerunner of SWCW, and dense SWCW—as "pure Soya Strait waters." Both the pure Soya Strait waters and those that have undergone modification and/or mixing are collectively referred to as "Soya Strait origin waters."

We considered two simple indices based on temperature and oxygen concentration (as well as salinity), because the SWCW is characterized by higher temperatures and oxygen concentrations than Kuril Basin waters at the same salinity (Takizawa, 1982). This feature is also observed in the Japan Sea Intermediate Water (e.g., Senjyu, 1999) and hence the pure Soya Strait waters.

To explain these indices, we first consider temperature-salinity (T-S) and apparent oxygen utilization-salinity (AOU-S) diagrams in Section 3.2.1, focusing on Soya Strait origin waters. AOU- and temperature-based indices are then introduced in Sections 3.2.2 and 3.2.3, respectively, to show the contribution of Soya Strait origin water to high-turbidity waters.

3.2.1 Water Properties of High-Turbidity Waters

In the T-S diagram (Fig. 4a), the Soya Strait origin waters are located in the region with higher temperature than the green curve and higher salinity than the green vertical line. The curve represents the upper temperature limit of the Kuril Basin water below the temperature minimum or dichothermal water (upper side of the black curve in December). The Kuril Basin subsurface water (that below the dichothermal water, e.g., $S > 33.1$) exhibited a relatively narrow and distinct T-S curve, particularly in December. Waters warmer than this curve were certainly classified as Soya Strait origin waters. Soya Strait origin waters were warm and clearly distinguished in December, whereas they were cold in April and began to warm in May. Note that the Kuril Basin water lighter than 26.8 σ_θ was colder in spring than in autumn. Accordingly, the water colder than the green curve may have included Soya Strait origin water, particularly in spring.

Figure 4b shows turbidity by color in the T-S diagram (waters with fluorescence > 0.3 or AOU < 0 are not colored). The figure confirms that high-turbidity waters were abundant in the range of Soya Strait origin water. Additionally, high-turbidity was observed in the dichothermal water (particularly those extending to relatively low densities correspond to the BML water near the shelf break in December, Fig. 2b) and bottom-contacting Kuril Basin subsurface water, primarily in the deeper regions of the S line (Fig. 3a, d).

In the AOU-S diagram (Fig. 4c), Soya Strait origin waters, identified in the T-S diagram, had lower AOU (higher oxygen concentrations) than the Kuril Basin subsurface water. Here, AOU was used instead of oxygen concentration to reduce temperature dependence (using oxygen or saturation gives similar results, see Appendix B). To clarify this correspondence, we marked waters in the higher temperature and salinity region with solid circles and the other regions with crosses in the diagrams. Most waters with lower AOU than the Kuril Basin water corresponded to these solid circles for S > 33.1, suggesting they were Soya Strait origin waters. The Kuril Basin subsurface water formed clear AOU-S curves extending from around S~33.2 and AOU~90 to higher AOU with increasing S. Lower AOU waters than these curves are the higher oxygen Soya Strait origin waters. For example, waters in December (black) with S > 33.1 and AOU < 80 were Soya Strait origin water. In April (blue), the temperature of Soya Strait origin water was similar to Kuril Basin water, but their AOU differed substantially. In fact, although waters near the dichothermal water in spring were colder than in December (green curve) and marked as crosses, many of these were in the low AOU range, identifying them as Soya Strait origin water. In the shallower layers (S < 33.1), the identification of the Soya Strait origin waters was complicated by oxygen oversaturation (AOU < 0) caused by phytoplankton blooms (Fig. 4c) and significant seasonal and interannual temperature variations (Fig. 4a). The green line was thus drawn at S = 33.1 to focus on the deeper layers.

Figure 4d shows turbidity in the AOU-S diagram as in Fig. 4b. The figure supports that high-turbidity water was abundant in low-AOU Soya Strait origin water. Turbidity color coding also helps to link the T-S and AOU-S diagrams. For example, high-turbidity waters in December (e.g., red in Fig. 4b, d) were of Soya Strait origin for S > 33.1, whereas for S < 33.1, warmer waters connected to the saline SWCW with lower AOU, and colder waters linked to the dichothermal water with higher AOU.

3.2.2 AOU-Based Index of Soya Strait Origin Waters

Since the differences in AOU were more pronounced than differences in temperature (especially in spring), we first considered an index based on AOU (and salinity). We aimed to distinguish waters with lower AOU than the Kuril Basin water at the same salinity for S > 33.1 as

Soya Strait origin waters. For this aim, we calculated the slope of the line in the AOU-S diagram connecting a reference point (green cross in Fig. 4c) to each data point:

$$(\Delta AOU/\Delta S)_i = (AOU_i - AOU_o)/(S_i - S_o) \qquad (1)$$

where the subscript i represents each data point, and o is the reference point. If the slope ΔAOU/ΔS is greater than that of the Kuril Basin subsurface water, it indicates lower AOU and therefore identifies the water as Soya Strait origin waters. This would be useful because the slope for the Kuril Basin subsurface water is relatively constant between the lower dichothermal water and the lower intermediate water ($33.1 \leq S \leq 34.1$).

The plot of ΔAOU/ΔS against salinity (Fig. 4e) shows that ΔAOU/ΔS generally increases monotonically for S < 33.2 but splits into two branches for S > 33.2. The lower branch, representing decreasing ΔAOU/ΔS, corresponds to the Kuril Basin subsurface water, with values ranging from 200 to 120 for S = 33.2 to 34.1. The upper branch, with increasing ΔAOU/ΔS, represents high-oxygen pure Soya Strait waters. Intermediate points between these branches are classified as Soya Strait origin waters. Thus, for S = 33.2–34.1, a ΔAOU/ΔS value greater than 200–120 generally indicates Soya Strait origin waters. The divergence near S = 34.15 is due to the reference point being set at S_o =34.15; for waters with S > 34.1, the reference point needs adjustment to identify Soya Strait origin waters.

The plot of ΔAOU/ΔS against turbidity (Fig. 4g) indicates that most of the relatively high-turbidity waters (say, > 0.2) were associated with ΔAOU/ΔS values greater than ~200, suggesting they were Soya Strait origin waters. Note that the figure excludes waters with fluorescence > 0.3, AOU < 0, or S > 34.1. High-ΔAOU/ΔS (≥200) water accounted for about 70% of high-turbidity water (≥ 0.2). This ratio increased with higher turbidity thresholds and lower ΔAOU/ΔS thresholds. The values and trends remained similar, even when the December observations were excluded. The above relation was also observed in vertical sections (Figs. 2 and 3). It was particularly clear in December, whereas in spring, it was clear over the shelf and off the Shiretoko Peninsula, with reasonable correspondence also seen offshore (a high ΔAOU/ΔS anomaly around 90 km on EW line in Fig. 2i was associated with AOU < 0). Thus, from both scatter plot and vertical sections, most of the high-turbidity water was identified as Soya Strait origin waters.

3.2.3 Temperature-Based Index of Soya Strait Origin Waters

We also considered a temperature-based index, as an AOU-based index may confuse the DSW with Soya Strait origin waters due to their similarly high oxygen levels. DSW or modified DSW is colder than the Kuril Basin water at the same salinity, making temperature a potentially distinguishing factor, unlike oxygen concentration. The temperature index aims to identify waters as Soya Strait origin waters if they are warmer than the Kuril Basin subsurface water at the same salinity. For this aim, we fitted a curve to the T-S distribution of the Kuril Basin water below the temperature minimum (purple line in Fig. 4a) and used the temperature difference between each data point and this curve ($\Delta\theta$) as the index:

$$\Delta\theta_i = \theta_i - \theta(Kuril\ Basin\ water)|_S \qquad (2)$$

The fitting curve was used because temperature differences in spring were too small compared to the temperature variability of the Kuril Basin water, for a slope-based index like the AOU-based index to distinguish the Soya Strait origin waters. The fitting curve (purple) was aligned with the lower portion of the T-S distribution of the Kuril Basin water (near the temperature lower limit). Specifically, it was aligned with the lower bound of the April distribution (blue) for $\sigma_\theta < 26.75$ (as winter mixing impacts up to this level) and gradually aligned with the lower bound of the December distribution (black) for $\sigma_\theta > 26.75$.

In the plot of $\Delta\theta$ against salinity (Fig. 4f), there was a little water with $\Delta\theta < 0$ at S = 33.4–33.7 (26.75–27.0 σ_θ). These low-temperature anomalies were weak and patchy in vertical sections (Fig. 2e) and likely caused by local winter mixing, though ruling out the possibility of modified DSW was difficult. Apart from these, the rest of the waters were identified as the Kuril Basin Water or the Soya Strait origin waters. The plot of $\Delta\theta$ against turbidity (Fig. 4h) shows that most of the high-turbidity waters (> 0.2) were associated with $\Delta\theta > 0.2$, indicating they were warmer than the Kuril Basin Water and were hence Soya Strait origin waters (similar to the AOU index). The high-turbidity waters with $\Delta\theta \sim 0$ corresponded to the dichothermal water contacting the shelf bottom (Figs. 2b and 4b) and aligned with high-turbidity waters with $\Delta AOU/\Delta S \sim 150$.

Thus, both AOU- and temperature-based indices identified most of the high-turbidity water as the Soya Strait origin waters. It follows that most of the high-turbidity water in the southwestern Kuril Basin originated from the Hokkaido shelf, including the dichothermal water in contact with the shelf bottom. It is worth noting that the AOU-based index is more convenient in spring when Soya Strait origin waters are colder, whereas the temperature-based index is more useful in autumn when these waters are warmer. In spring, the temperature was similar for Soya Strait origin water and Kuril Basin subsurface water, so that temperature-based identification is sensitive to the fitting curve choice. The green curve (one of the temperature-based indices) may misidentify colder Soya Strait origin water in spring as Kuril Basin water, whereas the purple curve may misidentify warmer Kuril Basin water in autumn as Soya Strait origin water. In addition, like the temperature-based index, the AOU-based index could be improved by fitting the Kuril Basin water's AOU-S curve, though its significant seasonal and interannual variations requires a fitting curve for each observation cruise (or each year or month). The $\Delta AOU/\Delta S$ index is convenient for use across different seasons and years, although the threshold should be adjusted slightly for each cruise and decreased with increasing salinity (density). Further, the above indices could be improved by standardization and analysis using past observation data, which are left for future work.

4. Bottom Mixed Layer on the Shelf

To better understand the distribution and spreading of high-turbidity water, we shift our focus to investigating the BML and the water within it, given the limited availability of turbidity data. We first utilize past observational data to show the distribution and seasonal variation of BML thickness and density (Section 4.1), which are compared with the BML in the model (Section 4.2), and then investigate the factors contributing to BML development using the model output.

4.1 Bottom Mixed Layer Estimated from Past Observation Data

The BML was defined here as the layer where the potential-density difference from the deepest layer observed does not exceed a threshold of 0.125 σ_θ (details in Appendix C), following the concept of the surface mixed layer (Levitus, 1982). After estimating the BML thickness for each station, we employed kriging to estimate the horizontal distribution of the BML for each season. The BML thickness and density are presented in Fig. 5. Note that in all seasons, the presence of small peaks and depressions suggests possible residual effects of disturbances. This was particularly so in winter due to the limited number of observations, which may have led to the influence of disturbances and monthly or yearly differences.

Throughout the year, the BML thickness reached a local maximum offshore of the SWC (20–50 km from the coast) near the region where the Cold Water Belt appears in summer (Fig. 5a, c, e, g). This is consistent with our observations (Fig. 2). This maximum was located between the strong density gradient along the coast associated with the SWC (e.g., Fig. 5d) and the Hokkaido side of the bottom streamline extending from the Soya Strait (red line). This maximum was thickest in spring (the area exceeding 60 m was largest in spring and almost absent in winter) and tended to develop downstream. The BML was also thick near the shelf break around the 300 m isobath (~144°E), particularly in autumn, although this peak is not pursued here due to the lack of data points.

The BML density also reached a maximum near the BML thickness maximum offshore of the SWC. This density maximum was slightly offshore (northeast) of the BML thickness maximum. The BML density at this maximum was highest in spring (~26.8 σ_θ), followed by summer (~26.7 σ_θ), autumn (~26.6 σ_θ), and winter (~26.6 σ_θ). The high spring and summer densities (> 26.7 σ_θ) correspond to the density range of the dense SWCW. The patchy anomalies with > 27 σ_θ in winter may be due to winter mixing or the Forerunner of SWCW, and the limited number of observation points.

These thick BML regions correspond to the regions where high-turbidity waters were observed, associated with thick BMLs (Fig. 2 and Wadaka 2008). In other words, the above analysis suggests that thick BMLs exist year-round with seasonal variations, and high-turbidity waters may also persist throughout the year.

4.2 Bottom Mixed Layer in the Model

The BML thickness in the model (Fig. 6a, d, g) is similar to the observations (Fig. 5), showing significant thicknesses offshore of the SWC and at the shelf break around 144°E. Note that the model analysis used a density threshold of 0.03 σ_θ (Thompson and Fine, 2003) instead of 0.125 σ_θ, as the higher threshold resulted in a thicker BML than observed, making it unsuitable for tracking BML waters, described in Section 5. For subsequent analyses, we focus on the offshore region of the SWC rather than the shelf break around 144°E, as the EW line observations (Fig. 2) show that the BML thickness at the shelf break was comparable to or less than that over the shelf. Additionally, the BML thickness may be increasingly overestimated with depth, as vertical grid spacing increases from 10 m at 200 m depth to 30 m at 300 m depth.

Figure 7 shows the seasonal variation in BML thickness and bottom density, salinity, and temperature averaged over the region where the BML thickened downstream along the offshore of the SWC (the square in Fig. 6a; 44.25–44.5°N, 144–144.3°E, near the EW line). The "bottom" in the model refers to the deepest grid hereafter. The BML thickness reached its maximum in May, minimum in January, and plateaued during summer. Bottom density and salinity exhibited similar variations, while bottom temperature differed slightly, peaking in August and reaching the minimum in February. We thus focus on January, May, and August to represent seasonal variations.

The BML thickness and bottom streamlines (Fig. 6a, d, g) indicate that the BML offshore of the SWC was dominated by water originating from the Japan Sea in all seasons. The BML developed as it flowed southeastward from the Soya Strait and exited the shelf toward Shiretoko near 144.3°E, where the shelf ends. Most of the BML water in and between the thick BML offshore of the SWC and the shelf break (45–46°N, 143.2–143.7°E) converged and then left the shelf. Likely due to this flow convergence, the BML thickened particularly at the point where it left the shelf near 44.25°N, 144.2°E.

Bottom density and salinity distributions (Fig. 6) support the idea that the thick BML is formed by water originating from the Japan Sea; the distribution of high-salinity water flowing from the Japan Sea matched the density maximum. Bottom density peaked offshore of the SWC, slightly offshore from the BML thickness maximum. This distribution and density values are consistent with the data analysis (Fig. 5). Salinity values were comparable in May and August, but higher temperatures in August lead to lower density, particularly for the warm SWCW along the coast. In January, despite low temperatures, density remained low due to reduced inflow of high-salinity water from the Japan Sea as the flow through the Soya Strait decreases in winter. The coastal region exhibited even lower salinity and density, likely because the shallow depth allows low-salinity ESC Water in the surface layer to reach the bottom.

4.3 Factors in Development of Bottom Mixed Layer

To consider the development of the BML, the vertical diffusivity (κ_z) 15 m above the bottom is shown in Fig. 8(a, d, g). The κ_z was large along the offshore side of the SWC, coinciding with the BML thickness maximum. This is consistent with the downstream development of the BML from the Soya Strait. Enhanced κ_z in the BML aligns with a previous observation in August (Ishizu et al. 2013). The large κ_z over shallow regions in January was due to wind-driven mixing reaching the bottom during winter storms.

Bottom current speeds (Fig. 8b, e, h), an indicator of shear production of turbulence at the bottom, were strong along the high-salinity, high-density water path from the Japan Sea, which coincided with the κ_z maximum. The bottom current speed did not align with the SWC axis, likely due to the buoyancy shutdown process, which weakens bottom currents (Karaki et al., 2018). Bottom currents were particularly strong from the Soya Strait to around 45.2°N, consistent with the seabed observations (Ikehara et al. 2001), and vertical diffusivity flux ($\kappa_z\,\partial\rho/\partial z$ where ρ is potential density) was also large in the Soya Strait (not shown). Seasonal variations of the flow through the Soya Strait influenced bottom current speeds, which were high in May and August and low in January. These suggest that bottom shear contributes to the development of the BML.

Further, we evaluated the buoyancy shutdown process, which was pointed out to develop the BML under the SWC (Karaki et al. 2018). In this process, the bottom Ekman transport associated with the SWC advects lower-density coastal water beneath higher-density offshore water, leading to a density inversion and the resulting development of the BML. To evaluate this process, we focused on horizontal density advection among terms causing density changes near the bottom and examined its vertical change:

$$\frac{\partial}{\partial t}\frac{\partial \rho}{\partial z} \sim -\frac{\partial}{\partial z}(\boldsymbol{u}_h \cdot \nabla\rho),$$

where $\boldsymbol{u_h}$ is horizontal current velocity and z is positive downward. If the right-hand side is negative, density stratification ($\partial\rho/\partial z$) weakens. Specifically, (1) when $\boldsymbol{u}_h \cdot \nabla\rho > 0$, bottom currents flow in the same direction as the density gradient, advecting lower-density water toward the higher-density side. (2) When $\partial/\partial z(\boldsymbol{u}_h \cdot \nabla\rho) > 0$, such a flow weakens as it moves away from the bottom as the bottom Ekman flow does, enabling lower-density water to subduct beneath higher-density water. We vertically integrated this equation for the bottom Ekman layer:

$$\frac{\partial}{\partial t}[\rho]_{Db}^{Db-\delta_E} \sim -[\boldsymbol{u}_h \cdot \nabla\rho]_{Db}^{Db-\delta_E} \;,$$

where z=Db represents the bottom depth, and δ_E is the thickness of the bottom Ekman layer. To reduce dependence on stratification strength, the right-hand side was divided by $\Delta\rho$, yielding the time scale T over which the density stratification changes, where $[\phi]_{Db}^{Db-\delta_E}$ is denoted as $\Delta\phi$, yielding:

$$1/T \sim \Delta(\boldsymbol{u}_h \cdot \nabla\rho)/\Delta\rho \qquad (3).$$

The sign was reversed to indicate the tendency toward density inversion for positive values. (Note that in a hydrostatic model, density inversion is immediately resolved.) Here, δ_E was set to 30 m (results were qualitatively similar for 20 m and 40 m).

The calculated $\Delta(\boldsymbol{u}_h \cdot \nabla\rho)/\Delta\rho$ (Fig. 8c, f, i) shows that the tendency to density inversion occurred primarily on the coastal side of the density maximum. Values were particularly large near the Soya Strait in May and August and along the whole density-maximum zone in May, but were much smaller in January. This temporal change is consistent with the seasonal variation in BML thickness, indicating its contribution to BML development.

Notably, the driving force of this effect differed from that of the buoyancy shutdown; $\Delta(\boldsymbol{u}_h \cdot \nabla\rho)/\Delta\rho$ occurred primarily along the onshore side of the density maximum (i.e., outside of the SWC), where the sea-surface horizontal pressure gradient is not the primary force except near the Soya Strait. A possible candidate is the bottom flow that extends the high-salinity water from the Japan Sea (Fig. 6f), which could be in turn due to a baroclinic wave propagating along the barotropic shear (Mitsudera et al. 2011). In addition, significant negative values were found, which is consistent with the mean bottom flow directed from the high-density side to the low-density side (particularly in August, Fig. 6h). This suggests the influence of a secondary circulation or eddies. In fact, the patchy distribution likely reflects the abundance of eddies along the Cold Water Belt.

As shown above, the development of the BML maxima was influenced by strong bottom currents from spring to autumn, with density destabilization caused by bottom currents also contributing in spring. Additionally, Fig. 6 (a, d, g) shows that the BML was thick in the Japan Sea when the BML offshore of the SWC was thick, indicating a possible contribution from the Japan Sea; when the BML is thick on the Japan Sea shelf, the stratification of the water inflowing into the bottom layer of the Okhotsk Sea weakens, making conditions favorable for BML development. On the other hand, a previous observation in August indicated that double-diffusion had a minor influence on κ_z, though it had a high potential in this region (Ishizu et al. 2013). Also, although bottom Ekman pumping associated with the SWC is another possible mechanism of BML development (Ishizu et al. 2008), its influence was minor in this model. Rather, where the BML was thick, the offshore component of bottom velocity diverged horizontally, as indicated by widening of bottom streamlines (142.3°–143.6°E in Fig. 6d, g), opposing Ekman pumping. This aligns with buoyancy shutdown, which suppresses bottom Ekman transport. Future observations are desired to confirm the dominant mechanism. It should be also emphasized that even the average bottom currents of 15–50 cm/s are sufficient to resuspend sediments, capable of eroding silt to medium-grain sand particles (Tanabe and Sakamoto, 2002; Pinet, 2000).

5. Spreading of Bottom Mixed Layer Water: Particle Tracking

This section attempts to reveal the spreading of high-turbidity water flowing out from the shelf using Lagrangian particle tracking. In doing so, since turbidity is not directly calculated in the model, the BML water was tracked as a proxy. Particles were initially placed within the BML on the shelf off the coast of Hokkaido in the Okhotsk Sea (Section 2.4) and tracked for one year. The case starting on August 1, 2012, is presented first to illustrate the general characteristics, followed by an examination of seasonal and interannual variability, as well as cases where particles had a sinking velocity.

5.1 Characteristics of Spreading and Density Dependence

Figure 9 shows the distribution of particle passage frequency over one year, categorized into three density ranges. The passage frequency indicates how the particles spread and their pathways, with higher values reflecting more particles passing through a given grid cell. Here, each particle was counted only once, even if it passed multiple times, recirculating through the same area. To illustrate density-related differences, initial densities were categorized as low (σ_θ < 26.0), intermediate (26.6 $\leq \sigma_\theta \leq$ 26.7), and high (σ_θ > 26.7). The low-density range (< 26.0) predominantly appeared near the coast (Fig. 6b, e, h) and represented the SWCW in summer to autumn and the ESC Water in winter. The high-density range (> 26.7) was found only near the density maximum offshore of the SWC, corresponding to the dense SWCW. The number of particles was 1,518, 7,471, and 4,013 for the low, intermediate, and high-density ranges, respectively, with the intermediate range having the largest volume.

The passage frequency distribution in the Kuril Basin was similar across density ranges, whereas the magnitude in the Kuril Basin and the pathways to the Pacific differed by density. Once in the Pacific, almost all particles flowed southwestward. Differences in passage frequency magnitude within the Kuril Basin reflected the initial volume (particle number) and the pathways to the Pacific, the latter affecting the time taken to reach the Pacific. Low-density range particles exited the Okhotsk Sea through closer, shallower straits such as the Kunashiri Strait and followed a more coastal path in the Pacific, though much fewer particles passed through the Nemuro Strait due to its too shallow depths (< 10 m). For higher density, a greater fraction exited through more distant and deeper straits, such as the Bussol Strait, with a higher proportion spreading throughout the Kuril Basin. The Etorofu Strait also served as a major pathway for intermediate-density particles.

The monthly passage frequencies for each density range (Fig. 10) show that the timescale of spreading and discharge to the Pacific depended on density. After one month (Fig. 10a, d, g), the BML water flowed off the shelf towards Shiretoko and began to spread along the archipelago. The low-density range water was outflowing actively through the Kunashiri Strait. After three months (Fig. 10b, e, h), the water spread throughout the western and central Kuril Basin. Most low-density water had already exited to the Pacific. For intermediate- and high-density waters, some particles started exiting through the Etorofu Strait and other eastern straits, but most remained in the Okhotsk Sea, with some still on the shelf. After five months (Fig. 10c, f, i), almost all low-density water had left the Okhotsk Sea. Intermediate- and high-density waters reached their peak outflow, though much remained in the Kuril Basin. In all density ranges, once BML waters left the shelf, they did not return.

To quantify the residence time in the Okhotsk Sea or the timescale for outflow to the Pacific, the time evolution of particle numbers in the Okhotsk Sea and the Pacific is plotted in Fig. 11a-c. Initially, all particles were in the Okhotsk Sea. As they flowed out to the Pacific, the number in the Okhotsk Sea decreased, whereas it increased in the Pacific. The time to outflow was clearly longer for higher-density particles. The outflow ratio after one year (number of particles in the Pacific after one year/initial number of particles) was lower for higher-density ranges, at 86%, 51%, and 39% for low-, intermediate-, and high-density ranges, respectively. Thus, roughly half or more of the intermediate- and high-density particles remained in the Okhotsk Sea for over one year. The time for half of the particles to exit also increased with density: 52 days for low, 352 days for intermediate, and > 365 days for high-density ranges. The faster outflow of low-density particles was due to their initial location in the swift SWC and their proximity to exit straits. Higher-density particles took longer to exit because they left through more distant straits and had a higher proportion that remained in the Kuril Basin for longer times.

5.2 Seasonal Variability

The previous section suggests that the outflow straits and residence time in the Okhotsk Sea differ by BML density. To investigate how this varies seasonally, particle tracking was conducted starting on the 1st of each month for one year.

The seasonal variability in pathways of BML waters is shown in Fig. 12 using the one-year passage frequency of particles across all density ranges for cases starting in January, May, and August, representing the seasonal variability. (Note that density ranges are not separated in Fig. 12 because some density ranges had no particles in certain months.) The pathways within the Okhotsk Sea were similar across seasons, with differences being smaller compared to interannual variability, as discussed later. However, the outflow paths to the Pacific varied due to seasonal changes in density. The BML water in winter mainly exited through the closer Kunashiri and

Etorofu Straits due to its low density. Spring BML water, with its higher density, primarily outflowed through the deeper Bussol Strait. Summer represented an intermediate case.

To examine seasonal variations in the time required for outflow to the Pacific, Figure 13 shows the outflow ratio after one year and the time taken for 50% of the particles to exit. Note that the low-density range during spring and high-density range in late autumn are not plotted due to their small particle number. Also, the months for which the time taken for 50 % to exit was longer than one year are not plotted.

The outflow ratio after one year (Fig. 13a) decreased with increasing density for all seasons. It was generally lowest for spring and highest for late autumn or early winter for all density ranges, though the range of seasonal variation was not large. The outflow ratio for the low-density range was 60–75% for winter and 80–90% for other seasons. It was 45–65% for the intermediate range, and 35–50% for the high-density range, with the remaining particles staying in the Okhotsk Sea after one year. The main reason for this seasonal variation was the difference in the frequency distribution of density within each range (not shown).

The time required for 50% of the particles to exit increased with density for all seasons (Fig. 13b). More than 50% remained almost year-round for the high-density range and from April to June for the intermediate range, so these periods are not plotted on the graph (months where more than 50% remained with sufficient particle numbers are blank in Fig. 13b but not in Fig. 13a). The intermediate range had the longest timescale for spring and nearly one year from winter to summer except for a local minimum for July, and the shortest for autumn at about six months. The short timescales for autumn and July were also associated with greater portions of lower density waters in this density range. For the low-density range, more than half of the particles exited to the Pacific within 2–3 months from summer to early winter.

In this way, the seasonal variability in the spreading of BML water was mainly caused by seasonal changes in density. The low-density range water exited rapidly to the Pacific throughout the year (slightly longer in winter), potentially affecting the surface layer of the Pacific. The intermediate-density range water, with about half remaining in the Okhotsk Sea after one year from March to July, stayed mostly until the next winter in other periods. This water could be entrained into the euphotic zone during winter mixing and contribute to the following spring bloom. The high-density range water stayed in the Okhotsk Sea for over one year, influencing the intermediate layer material circulation, and could potentially be transported to the euphotic zone by tidal mixing in the Kuril Straits.

5.3 Interannual Variability

To examine interannual variability, particle tracking of BML water was conducted for one year starting from August 1st each year from 2008 to 2016. To reduce computation time, this was done on the 26.6 isopycnal surface, so that interannual variability in density only affected the number of particles.

Interannual variability was large for pathways (Fig. 14) but small for the outflow timescale (Fig. 15). The passage frequency distribution for each year (Fig. 14) shows that in all years, BML water initially moved along the SWC over the shelf off Hokkaido and exited into the Kuril Basin west of the Shiretoko Peninsula, often forming eddies north of Etorofu Island. However, interannual variability was much larger than seasonal variability. In some years, most of the water remained in the western and central Kuril Basin, whereas in other years, it spread significantly northward. Since the initial density was the same, this variability was primarily due to changes in the flow field. Interannual variability was also observed for the outflow ratio to the Pacific after one year even with the same density (Fig. 15). Though it was not large (excluding 2011, it fluctuated within ±5% around 35%), it could be increased by the interannual variations in BML density.

5.4 Effects of Sinking Velocity

Thus far, suspended particles were assumed to be small enough that sinking velocity can be ignored. In reality, large, suspended particles have significant sinking velocities. To investigate the effects of sinking, we assigned a sinking velocity to the tracked particles, except for the bottommost grid where particles were assumed to stop sinking or be resuspended due to turbulence. Two cases, with sinking velocities of 0.4 m/day and 4 m/day, are presented as examples of slow and fast-sinking particles.

Differences due to sinking velocity were clearly reflected in the time evolution of the number of particles in the Okhotsk Sea and the Pacific, categorized by initial density range (Fig. 11d-i). As sinking particles gradually moved into higher-density layers, their behavior shifted to that of higher-density particles. Even with a sinking velocity of 0.4 m/day, the time required for outflow increased by 10–20% (sinking 73 m over six months apart from advection). A sinking velocity of 4 m/day causes particles to descend 120 m in one month and 730 m in six months, independent of advection, preventing their escape through shallow straits after one month and effectively trapping them within the Okhotsk Sea after six months. These particles likely accumulate or undergo remineralization within the Okhotsk Sea. Thus, while slow-sinking particles behaved similarly to those described in Sections 5.1-5.3, fast-sinking particles exhibited qualitatively different behavior.

6. Summary and Discussion

The region extending from the Hokkaido coast to the Kuril Basin in the Okhotsk Sea is characterized by high primary production, which supports high biodiversity and productive fisheries. This study focused on high-turbidity water in the BML on the shelf off Hokkaido, as a component of nutrient cycling.

Observations conducted in April, May, and December revealed that high-turbidity water and a thick BML on the shelf off Hokkaido were present not only in August, as previously observed, but also in spring and late autumn. Most of the high-turbidity water in the southwestern Kuril Basin was Soya Strait origin waters, entering from the Japan Sea and passing over the Hokkaido shelf.

Analysis of past data revealed the seasonal distribution of BML thickness and density. BML thickness peaked offshore of the SWC (20–50 km from the coast), coinciding with the location of the Cold-Water Belt, which forms in spring to autumn. Both BML thickness and density were highest in spring and lowest in winter. The thick BML observed during the cruises is likely present year-round, albeit with seasonal variability, suggesting that high-turbidity water may also persist.

An output from the JPN system developed by MRI of the JMA indicated similar patterns in BML thickness and density. The water mass with the thickest BML originated from the Japan Sea. The seasonal development of the BML was primarily driven by strong bottom currents around the Soya Strait, density destabilization by bottom currents, and the BML development in the Japan Sea.

As a proxy for high-turbidity water, we tracked water within the BML using the JPN system output. Low-density water ($\sigma_\theta < 26.0$) rapidly exited to the Pacific Ocean via nearby shallow straits like the Kunashiri Strait, with a small proportion remaining in the Okhotsk Sea after one year (half of the particles exited within 2–3 months, and only 14% remained after one year). In contrast, higher-density water took longer to exit through distant deeper straits like the Bussol Strait, resulting in a higher proportion remaining and spreading within the Kuril Basin (for water with $\sigma_\theta > 26.7$, 60% remained in the Okhotsk Sea after one year). The extent of spread within the Okhotsk Sea exhibited smaller seasonal variability compared to interannual variability, with the outflow ratio to the Pacific Ocean after one year fluctuating with the seasonal changes of the BML density. Interannual variability in current fields significantly altered the spread within the Okhotsk Sea. When sinking velocities were assigned, slow-sinking particles ($\lesssim$ 0.4 m/day) behaved similarly to the above neutrally buoyant particles, whereas fast-sinking particles ($\gtrsim$ 4 m/day) exhibited qualitatively different behavior.

The above results suggest the following: high-turbidity bottom waters off the Hokkaido coast in the Okhotsk Sea are transported to the Kuril Basin and the North Pacific (southeast of Hokkaido in particular), potentially influencing the material circulation. High-turbidity bottom waters of low density rapidly exit to the Pacific Ocean, affecting the coastal euphotic zone. High-turbidity bottom waters of intermediate density remain in the Okhotsk Sea until the following winter, where they may contribute to the spring bloom after being mixed into the euphotic zone by winter convection. High-turbidity bottom waters of high density remain in the Okhotsk Sea for over a year, potentially influencing the intermediate layer and benthic material circulation and ecosystems, remaining suspended or sinking. It may also affect the euphotic zone through entrainment by tidal mixing.

It should be noted that this study did not directly investigate the fate of the high-turbidity water but instead tracked BML water. Observations and modeling of turbidity or suspended particles are desired. The effects of storm events, which can effectively resuspend sediments and increase turbidity, were not considered in the particle tracking analysis in Section 5. Additionally, it is desired to explore how nutrients in suspended particles transform into bioavailable forms. These are left for future work.

Appendix A: Model flow field and water mass structure

Appendix A shows the flow field and water mass structures in the model used. Figure A1 presents the monthly-mean, near-surface flow field during 2008-2017. Although the flow field was complex with many eddies, its main features qualitatively consistent with observational knowledge: (1) the ESC strengthened in winter and weakened in summer, with a coastal branch extending to Hokkaido during winter; (2) the SWC intensified in summer, with parts of both the ESC and SWC flowing into the North Pacific via straits near Hokkaido such as the Kunashiri Strait, forming the Coastal Oyashio along southeastern Hokkaido; and (3) the Oyashio and water exchange between the Okhotsk Sea and the North Pacific strengthened in winter. Additionally, a relatively large anticyclonic eddy in the Kuril Basin was consistent with observational findings.

Figure A2a shows a T-S diagram for January, May, and August around the EW line. Temperature, salinity, and density distributions were qualitatively well-reproduced. Key features include (1) the Kuril Basin water below 26.7 $\sigma\theta$, the dichothermal water, and their gradual warming from early summer; (2) the warm and saline SWCW and low-salinity Kuril Basin surface water in early and late summer; and (3) the low-salinity ESC Water in winter. Additionally, a T-S diagram for April, May, and December (Fig. A2b), provided for comparison with Fig. 4a, showed remarkable agreement with observations despite interannual variability.

Appendix B: Identifying Soya Strait Origin Waters Using Dissolved Oxygen and Oxygen Saturation

Section 3.2 identified the Soya Strait origin waters using AOU and temperature-based indices, as the Soya Strait origin waters are characterized by higher oxygen concentrations and temperatures compared to Kuril Basin water. Here, we compare the AOU-based method with methods based on dissolved oxygen (O) and oxygen saturation (S_{O2}), where the latter was calculated at sea surface pressure.

Figures B1a-d present S_{O2}-S and O-S diagrams alongside T-S and AOU-S diagrams for comparison. The S_{O2}-S plot (Fig. B1d) closely mirrored an inverted AOU-S plot (Fig. B1b), resulting in nearly identical outcomes when calculating $\Delta S_{O2}/\Delta S$ compared to $\Delta AOU/\Delta S$. Indeed, the plots of both $-\Delta S_{O2}/\Delta S$ vs. S (Fig. B1f) and $-\Delta S_{O2}/\Delta S$ vs. turbidity (Fig. B1h) were nearly identical to those for $\Delta AOU/\Delta S$ (Fig. 4e, g). (The negative sign for $\Delta S_{O2}/\Delta S$ was added to match the sign convention used for $\Delta AOU/\Delta S$.)

On the other hand, the O-S plot shows significant temperature-dependence above the dichothermal water. In particular, the less-saline surface layer ($S \lesssim 33$) exhibited large variability depending on the observation month/year. Further, although the T-S curve consisting of the surface water, the SWCW, and the subsurface Kuril Basin water in December resembles a tilted 'Z' shape, the upper horizontal and diagonal lines of the 'Z' overlapped in the O-S diagram, forming a single line. (In the AOU-S and S_{O2}-S diagrams, these lines remained separate.)

Figure B1e shows $-\Delta O/\Delta S$ vs. S plot. The temperature-dependent variability caused larger differences between years and months compared to the $\Delta AOU/\Delta S$ plot, especially for the less-saline surface water ($S \lesssim 33$) and, to some extent for the upper branch of $S > 33.2$. However, despite this variability, the differences did not practically affect the identification of Soya Strait origin waters, and the overall results (Fig. B1g) were similar to those obtained using the AOU-based index.

Appendix C: Estimation Method for the Bottom Mixed-Layer Thickness

The BML was defined as the layer where the density difference from the deepest layer observed does not exceed a threshold of 0.125 σ_θ. Specifically, the lower boundary of the interior (D_i) was defined where potential density first exceeded the threshold relative to the deepest layer observed (D_o), and the upper boundary of the BML (D_u) was defined as the observed layer immediately below the lower boundary. BML thickness was then calculated as the distance from the depth of the upper boundary to the bottom (D_b-D_u, Fig. C1).

When the deepest layer observed was away from the bottom, BML thickness could not be accurately assessed. Therefore, we checked the relationship between the distance from the bottom (D_b-D_o) and the estimated BML thickness (D_b-D_u). At observation sites where $D_b-D_o \leq 50$ m, D_b-D_u varied continuously from 0 to 200 m. However, at sites where $D_b-D_o > 50$ m, D_b-D_u varied discretely (Fig. C2), indicating the possible influence of D_b-D_o on estimated BML thickness. Consequently, we excluded sites where $D_b-D_o > 50$ m from the analysis. The number of excluded sites was minimal, accounting for less than 2% of the total (Table C1).

Acknowledgments

We are grateful to the Meteorological Research Institute (MRI), JMA for providing an output of the JPN system and the Hokkaido Research Organization (HRO) and Japan Oceanographic Data Center (JODC) for their observation data archive. We also thank the captain, officers, crews and onboard scientists of R/V Hakuho-Maru (KH-20-12) and Shinsei-Maru (KS-21-06, KS-22-06) cruises, which were supported by AORI and JAMSTEC (JURCAOSS20-22, JURCAOSS21-15, JURCAOSS22-19). This study was supported by JSPS KAKENHI Grant Numbers JP21K03655, JP20H03054, JP22H05204, JP21H05056, the Environment Research and Technology Development Fund (JPMERF20214002) of the Environmental Restoration and Conservation Agency of Japan, AORI Interdisciplinary Collaborative Research, and Pan-Okhotsk Collaboration Project and Joint Research Program (22S010, 23S015) of the Institute of Low Temperature Science, Hokkaido University. Some of the figures were drawn using GrADS, and the main calculations and analyses were conducted with ILTS Information System. We also thank anonymous reviewers for their valuable comments.

Data Availability

The observation data archived by JODC and the output of JPN system are available through the web sites (https://www.jodc.go.jp/jodcweb/JDOSS/index_j.html, https://search.diasjp.net/ja/dataset/MOVEJPN_MRI_2020). The observation data in section 3 and those archived by HRO are available from Dr. Tomohiro Nakamura (KH-20-12, KS-22-06) and Jun Nishioka (KS-21-06), and HRO, respectively, upon request under certain conditions.

References

Aldama-Campino, A., Doos, K., Kjellsson, J., Jonsson, B. (2020). TRACMASS: Formal release of version 7.0 (Version v7.0-beta). Zenodo. http://doi.org/10.5281/zenodo.4337926

Aota, M. (1975): Studies on the Soya Warm Current. Low Temp. Sci. Ser. A. 33, 151-172, http://hdl.handle.net/2115/18282 (In Japanese with an English summary)

Chiba, A., Horio, K., Isoda, Y., Kobayashi, N. (2021) Transport and alteration processes of dense Soya Current Water at the shelf-basin boundary off Abashiri. Oceanography in Japan 30, 15-46. doi: 10.5928/kaiyou.30.2_15 (In Japanese with an abstract and figure captions in English.)

Danchenkov, M. A., Aubrey, D., Riser, S. C. (1999): Oceanographic feature of LaPerouse Strait. PICES Scientific Report No.12, 159-171.

Doos K., Kjellsson J., Jonsson B. (2013) TRACMASS - A Lagrangian Trajectory Model. In: Soomere T., Quak E. (eds) Preventive Methods for Coastal Protection. Springer, Heidelberg. https://doi.org/10.1007/978-3-319-00440-2_7

Doos, K., Jonsson, B., Kjellsson, J. (2017), Evaluation of oceanic and atmospheric trajectory schemes in the TRACMASS trajectory model v6.0, Geoscientific Model Development, 10(4), 1733-1749, 10.5194/gmd-10-1733-2017

Ebuchi, N. (2006) Seasonal and interannual variations in the East Sakhalin current revealed by TOPEX/POSEIDON altimeter data. J Oceanogr 62, 171-183, doi.org/10.1007/s10872-006-0042-x

Ebuchi N, Fukamachi Y, Ohshima KI, Shirasawa K, Ishikawa M, Takatsuka T, Daibo T, Wakatsuchi M (2006) Observation of the Soya Warm Current using HF radar. J. Oceanogr. 62, 47-61, doi.org/10.1007/s10872-006-0031-0

Ebuchi, N., Fukamachi, Y., Ohshima, K.I., Mitsudera, H., Nishioka, J., Takatsuka, T., Ono, K., Ishikawa, M., Daibo, T., Shirasawa, K., Wakatsuchi, M. (2024) Long-term observation of the Soya Warm Current using HF ocean radars: relationship between the Soya Warm Current variability and the sea level anomalies in the Soya/La Perouse Strait. J Oceanogr 80, 239–249. https://doi.org/10.1007/s10872-024-00724-w

Fukamachi YI, Tanaka KI, Ohshima N, Ebuchi G, Mizuta H, Yoshida ST, Wakatsuchi M (2008) Volume transport of the Soya Warm Current revealed by bottom-mounted ADCP and ocean-radar measurement. J Oceanogr 64, 385-392, doi.org/10.1007/s10872-008-0031-3

Hirose, N., N. Usui, K. Sakamoto, H. Tsujino, G. Yamanaka, H. Nakano, S. Urakawa, T. Toyoda, Y. Fujii, N. Kohno, 2019: Development of a new operational system for monitoring and forecasting coastal and open ocean states around Japan. Ocean Dyn., 69, 1333-1357. https://doi:10.1007/s10236-019-01306-x

Iida, H., Isoda, Y., Kobayashi, N., Horio, K. (2018) Observations and model experiments of the diurnal eddy of the Cold Water Belt along the offshore side of the Soya Warm Current. Oceanography in Japan, 27, 155-174, doi: 10.5928/kaiyou.27.4_155. (In Japanese with an abstract and figure captions in English)

Ikehara, K., Katayama, H., Noda, A. (2001a) VII Seafloor characteristics in the area extending from the Soya Strait to the Kitami-Yamato Bank based on seafloor photographs. GSJ Interim Report no. MB/01/1, 71-77. (in Japanese with figure legends in English)

Ikehara, K., Noda, A., Katayama, H., Maekawa, T. (2001b) VIII Surface sediments in the area extending from the Soya Strait to the Kitami-Yamato Bank. GSJ Interim Report no. MB/01/1, 78-90. (in Japanese with figure legends in English)

Imai, M. (2023) Biogeochemical environment and impact of material supply following sea ice melt in the Okhotsk Sea. Master thesis, Hokkaido University

Inoue, S. (2021) Ocean circulation and its variability in the Nemuro Strait. Master thesis, Hokkaido University

Itoh, M., Ohshima, K. I. (2000) Seasonal variations of water masses and sea level in the southwestern part of the Okhotsk Sea. J. Oceanogr. 56 (6), 643-654.

Itoh, S., Yasuda, I., Yagi, M., Osafune, S., Kaneko, H., Nishioka, J., ... & Volkov, Y. N. (2011). Strong vertical mixing in the Urup Strait. Geophysical research letters, 38(16). https://doi.org/10.1029/2011GL048507

Ishizu, M., Kitade, Y., Matsuyama, M. (2006) Formation mechanism of the cold-water belt formed off the soya warm current. J Oceanogr 62, 457–471. https://doi.org/10.1007/s10872-006-0068-0

Ishizu, M., Kitade, Y., Matsuyama, M. (2008) Characteristics of the cold-water belt formed off Soya Warm Current. J. Geophys. Res. 113, C12010, doi:10.1029/2008JC004786.

Ishizu, M., Kitade, Y., Michida, Y. (2013) Mixing process on the northeast coast of Hokkaido in summer. J Oceanogr 69, 1–13. https://doi.org/10.1007/s10872-012-0152-6

Kanna, N., Sibano, Y., Toyota, T., Nishioka, J. (2018) Winter iron supply processes fueling spring phytoplankton growth in a sub-polar marginal sea, the Sea of Okhotsk: Importance of sea ice and the East Sakhalin Current. Marine Chemistry 206, 109-120, doi.org/10.1016/j.marchem.2018.08.006

Karaki, T., Mitsudera, H., Kuroda, H. (2018) Buoyancy shutdown process for the development of the baroclinic jet structure of the Soya Warm Current during summer. J Oceanogr 74, 339-350. https://doi.org/10.1007/s10872-018-0465-1

Kasai, H., Nakano, Y., Ono, T., Tsuda, A. (2010) Seasonal change of oceanographic conditions and chlorophyll a vertical distribution in the southwestern Okhotsk Sea during the non-iced season. J. Oceanogr. 66, 13-26, doi.org/10.1007/s10872-010-0002-3

Katayama, H., Noda, A., Ikehara, K. (2002) V. Ocean environment off Abashiri in the Okhotsk Sea. GSJ Interim Report no. 25, 46-57. (in Japanese with figure legends in English)

Katsumata, K., Ohshima, K. I., Kono, T., Itoh, M., Yasuda, I., Volkov, Y. N., Wakatsuchi, M. (2004) Water exchange and tidal currents through the Bussol' Strait revealed by direct current measurements, J. Geophys. Res., 109, C09S06, doi:10.1029/2003JC001864

Kishi, S., Ohshima, K. I., Nishioka, J., Isshiki, N., Nihashi, S., Riser,S. C. (2021) The prominent spring bloom and its relation to sea-ice melt in the Sea of Okhotsk, revealed by profiling floats. Geophys. Res. Letters, 48, e2020GL091394, doi.org/10.1029/2020GL091394

Kitani, K. (1973), An oceanographic study of the Okhotsk Sea-Particularly in regard to cold waters, Bull. Far Seas Fish. Res. Lab., 9, 45-77.

Kobayashi, S., Y. Ota, Y., Harada, Y., Ebita, A., Moriya, M., Onoda, H., Onogi, K., Kamahori, H., Kobayashi, C., Endo, H., Miyaoka, K., Takahashi, K. (2015) The JRA-55 reanalysis: general specifications and basic characteristics. J. Meteor. Soc. Japan, 93, 5–48. https://doi.org/10.2151/jmsj.2015-001

Kono, T., Kawasaki, Y. (1997). Modification of the western subarctic water by exchange with the Okhotsk Sea. Deep Sea Research Part I: Oceanographic Research Papers, 44(4), 689-711.

https://doi.org/10.1016/S0967-0637(96)00107-0

Kono, T., Sato, M. (2010) A mixing analysis of surface water in the Oyashio region: Its implications and application to variations of the spring bloom. Deep Sea Research Part II, 57, 1595-1607. https://doi.org/10.1016/j.dsr2.2010.03.004

Kudo, I., Aya, F., Takata, H., Kobayashi, N. (2011) Oceanographic structure and biological productivity in the coastal area of Okhotsk Sea. Bull. Coast. Oceanogr. 49, 13-21. (in Japanese with an abstract and figure captions in English).

Kuma, K., Sasayama, R., Hioki, N., Morita, Y., Isoda, Y., Hirawake, T., Imai, K., Aramaki, T., Nakamura, T., Nishioka, J., Ebuchi, N. (2014) Chemical evidence for the origin of the cold water belt along the northeastern coast of Hokkaido. J. Oceanogr. 70, 377-387, doi.org/10.1007/s10872-014-0239-3

Kurashina, S., Nishida, K., Nakabayashi, S. (1967), On the open water in the southeastern part of the frozen Okhotsk Sea and the currents through the Kuril Islands (in Japanese with abstract and figure captions in English), J. Oceanogr. Soc. Jpn., 23, 57-62.

Kuroda, H., Toya, Y., Watanabe, T., Nishioka, J., Hasegawa, D., Taniuchi, Y., Kuwata, A. (2019) Influence of Coastal Oyashio water on massive spring diatom blooms in the Oyashio area of the North Pacific Ocean. Progress in Oceanography, 175, 328-344. https://doi.org/10.1016/j.pocean.2019.05.004

Levitus, S., (1982) Climatological Atlas of the World Ocean. NOAA Prof. Paper 13, 173 pp.

Matsuyama, M., Wadaka, M., Abe, T., Aota, M., Koike, Y. (2006) Current structure and volume transport of the Soya Warm Current in summer. J. Oceanogr. 62, 197-205, doi.org/10.1007/s10872-006-0044-8

Mensah, V., Ohshima, K.I., Nakanowatari, T., Riser, S. (2019) Seasonal changes of water mass, circulation and dynamic response in the Kuril Basin of the Sea of Okhotsk. Deep Sea Res. Part I 144, 115-131, doi.org/10.1016/j.dsr.2019.01.012

Mitsudera, H., Uchimoto, K., Nakamura, T. (2011) Rotating stratified barotropic flow over topography: mechanisms of the cold belt formation off the Soya Warm Current along the northeastern coast of Hokkaido. J. Phys. Oceanogr. 41, 2120-2136, doi.org/10.1175/2011JPO4598.1.

Miura, T., Suga, T., Hanawa, K. (2002). Winter mixed layer and formation of dichothermal water in the Bering Sea. Journal of Oceanography, 58, 815-823. https://doi.org/10.1023/A:1022871112946

Mizuta, G., Fukamachi, Y., Ohshima, K.I., Wakatsuchi, M. (2003) Structure and seasonal variability of the East Sakhalin Current. J. Phys. Oceanogr. 33, 2430-2445.

Mundo, R., Matsunaka, T., Nakanowatari, T., Taniuchi, Y., Inoue, M., Kasai, H., Mashita, K., Mitsunushi, H., Nagao, S. (2024) A review of the oceanographic structure and biological productivity in the southern Okhotsk Sea. Progress in Oceanography, 221, 103194. doi.org/10.1016/j.pocean.2023.103194.

Mustapha, M. A., Sei-Ichi, S., Lihan, T. (2009) Satellite-measured seasonal variations in primary production in the scallop-farming region of the Okhotsk Sea. ICES Journal of Marine Science, 66: 1557-1569, doi:10.1093/icesjms/fsp142

Nakamura, T., Awaji, T., Toyoda, T., Ishikawa, Y. (2003) Coastal Oyashio in a North Pacific simulation experiment. Bulletin on Coastal Oceanography, 41, 13-22. https://doi.org/10.32142/engankaiyo.41.1_13 (in Japanese with an abstract and figure captions in English.)

Nakamura, T., Awaji, T. (2004) Tidally induced diapycnal mixing in the Kuril Straits and its role in water transformation and transport: a three-dimensional nonhydrostatic model experiment. J. Geophys. Res. 109, C09S07, doi.org/10.1029/2003JC001850.

Nakamura, T., Toyoda, T., Ishikawa, Y., Awaji, T. (2006). Effects of tidal mixing at the Kuril Straits on North Pacific ventilation: Adjustment of the intermediate layer revealed from numerical experiments. Journal of Geophysical Research: Oceans, 111(C4). https://doi.org/10.1029/2005JC003142

Nakanowatari, T., Nakamura, T., Uchimoto, K., Nishioka, J., Mitsudera, H., Wakatsuchi, M. (2017). Importance of E kman transport and gyre circulation change on seasonal variation of surface dissolved iron in the western subarctic N orth P acific. Journal of Geophysical Research: Oceans, 122(5), 4364-4391. https://doi.org/10.1002/2016JC012354

Nakatsuka, T., Fujimune, T., Yoshikawa, C., Noriki, S., Kawamura, K., Fukamachi, Y., ... Wakatsuchi, M. (2004). Biogenic and lithogenic particle fluxes in the western region of the Sea of Okhotsk: Implications for lateral material transport and biological productivity. Journal of Geophysical Research: Oceans, 109(C9). https://doi.org/10.1029/2003JC001908

Nakatsuka, T., Toda, M., Kawamura, K., Wakatsuchi, M. (2004). Dissolved and particulate organic carbon in the Sea of Okhotsk: Transport from continental shelf to ocean interior. Journal of Geophysical Research: Oceans, 109(C9). https://doi.org/10.1029/2003JC001909

Nishioka, J., Obata, H., Ogawa, H., Ono, K., Yamashita, Y., Lee, K., Takeda, S., Yasuda, I. (2020). Subpolar marginal seas fuel the North Pacific through the intermediate water at the termination of the global ocean circulation. Proceedings of the National Academy of Sciences, 117(23), 12665-12673. https://doi.org/10.1073/pnas.2000658117

NOAA National Geophysical Data Center. 2009: ETOPO1 1 Arc-Minute Global Relief Model. NOAA National Centers for Environmental Information.

Noda, A., Ikehara, K., Katayama, H., Maekawa, T. (2001) VI Ocean environment in the area extending from the Soya Strait to the Kitami-Yamato Bank. GSJ Interim Report no. MB/01/1, 57-70. (in Japanese with figure legends in English)

Noda, A., Katayama, H., Ikehara, K. (2002) VI. Seafloor characteristics in the area extending from offshore Abashiri to the Kitami-Yamato Bank based on seafloor photographs. GSJ Interim Report no. 25, 58-62. (in Japanese with figure legends in English)

Noda, A., Katayama, H., Ikehara, K. (2002) VII. Surface sediments in the area extending from offshore Abashiri to the Kitami-Yamato Bank. GSJ Interim Report no. 25, 63-72. (in Japanese with figure legends in English)

Ohshima, K.I., Wakatsuchi, M., Fukamachi, Y., Mizuta, G. (2002) Near-surface circulation and tidal currents of the Okhotsk Sea observed with satellite-tracked drifters. J. Geophys. Res. Oceans 107 (C11), 16-21.

Ohshima, K.I., Nakanowatari, T., Riser, S., Wakatsuchi, M. (2010) Seasonal variation in the in- and outflow of the Okhotsk Sea with the North Pacific. Deep Sea Res. Part II, 57, 1247-1256. doi.org/10.1016/j.dsr2.2009.12.012.

Ohshima KI, Simizu D, Ebuchi N, Morishima S, Kashiwase H (2017) Volume, Heat, and Salt Transports through the Soya Strait and Their Seasonal and Interannual Variations. J. Phys. Oceanogr., 47, 999-1019, doi.org/10.1175/JPO-D-16-0210.1.

Pinet, P. R. (2000) Chapter 4 Marine Sedimentation, Invitation to Oceanography, Second Edition, Jones and Bartrett Publishers

Sakamoto K, Tsujino H, Nishikawa S, Nakano H, Motoi T (2010) Dynamics of the Coastal Oyashio and its seasonal variation in a high-resolution Western North Pacific Ocean model. J. Phys. Oceanogr. 40 (6), 1283-1301

Sakamoto, K., Tsujino, H., Nakano, H., Hirabara, M., Yamanaka, G. (2013) A practical scheme to introduce explicit tidal forcing into an OGCM. Ocean Sci., 9, 1089-1108. https://doi.org/10.5194/os-9-1089-2013

Sakamoto, K., Tsujino, H., Nakano, H., Urakawa, S., Toyoda, T., Hirose, N., Usui, N., Yamanaka, G. (2019) Development of a 2km-resolution ocean model covering the coastal seas around Japan for operational application. Ocean Dyn., 69, 1181-1202. https://doi.org/10.1007/s10236-019-01291-1

Senjyu, T. The Japan Sea Intermediate Water; Its Characteristics and Circulation. Journal of Oceanography 55, 111-122 (1999). https://doi.org/10.1023/A:1007825609622

Suzuki, T., D. Yamazaki, H. Tsujino, Y. Komuro, H. Nakano, S. Urakawa, 2018: A dataset of continental river discharge based on JRA-55 for use in a global ocean circulation model. J. Oceanogr., 74, 421-429. https://doi.org/10.1007/s10872-017-0458-5

Takizawa, T. (1982) Characteristics of the Soya warm current in the Okhotsk Sea. J. Oceanogr. Soc. Jpn. 38 (5), 281-292.

Tanabe, T., Sakamoto, T. (2002) VIII. Grain size, mineral composition, and provenance of terrestrial clastic materials in surface sediments from the southwestern Okhotsk Sea, collected during the GH00 and GH01 cruises. GSJ Interim Report no. 25, 73-98 (in Japanese with figure legends in English).

Thomson, R. E., Fine,I. V., (2003) Estimating mixed layer depth from oceanic profile data. J. Atmos. Oceanic Technol., 20, 319-329, https://doi.org/10.1175/1520-0426(2003)020,0319:EMLDFO.2.0.CO;2.

Tsujino, H., Nakano, H., Sakamoto, K., Urakawa, S., Hirabara, M., Ishizaki, H., Yamanaka, G. (2017) Reference manual for the Meteorological Research Institute Community Ocean Model version 4 (MRI.COMv4). Tech. Rep., 80, Meteorological Research Institute, Japan. https://doi.org/10.11483/mritechrepo./80

Tsujino, H., Urakawa, S., Nakano, H., Small, R. J., Kim, W. M., Yeager, S. G., Danabasoglu, G., Suzuki, T., Bamber, J. L., Bentsen, M., Boning, C. W., Bozec, A., Chassignet, E. P., Curchitser, E., Dias, F. B., Durack, P. J., Griffies, S. M., Harada, Y., Ilicak, M., Josey, S. A., Kobayashi, C., Kobayashi, S., Komuro, Y., Large, W. G., Sommer, J. L., Marsland, S. J., Masina, S., Scheinert, M., Tomita, H., Valdivieso, M., Yamazaki, D. (2018) JRA-55 based surface dataset for driving ocean-sea-ice models (JRA55-do). Ocean Modell., 130, 79-139. https://doi.org/10.1016/j.ocemod.2018.07.002

Uchimoto, K., Nakamura, T., Nishioka, J., Mitsudera, H., Yamamoto-Kawai, M., Misumi, K., Tsumune, D. (2011). Simulations of chlorofluorocarbons in and around the Sea of Okhotsk: Effects of tidal mixing and brine rejection on the ventilation. Journal of Geophysical Research: Oceans, 116(C2). https://doi.org/10.1029/2010JC006487

Uehara, H., Kruts, A. A., Volkov, Y. N., Nakamura, T., Ono, T., Mitsudera, H. (2012). A new climatology of the Okhotsk Sea derived from the FERHRI database. Journal of oceanography, 68, 869-886. https://doi.org/10.1007/s10872-012-0147-3

Wadaka, M. (2008) Study on high-turbidity water formed in the bottom layer on the offshore side of the Soya Warm Current. Ph.D thesis, Tokyo University of Marine Science and Technology, http://id.nii.ac.jp/1342/00000789 (in Japanese with figure captions in English).

Wadaka, M., Matsuyama, M., Ishizu, M., Kitade, Y., Yano, Y. (2009) Bottom high turbidity water observed off the Soya Warm Current in the Okhotsk Sea. Bull. Coastal Oceanography, 46, 175-183. (in Japanese with an abstract and figure captions in English)

Wakatsuchi, M., Martin, S. (1991) Water circulation in the Kuril Basin of the Okhotsk Sea and its relation to eddy formation. J. Oceanogr. Soc. Jpn. 47, 152-168.

Warner, M. J., Bullister, J. L., Wisegarver, D. P., Gammon, R. H., Weiss, R. F. (1996). Basin-wide distributions of chlorofluorocarbons CFC-11 and CFC-12 in the North Pacific: 1985-1989. Journal of Geophysical Research: Oceans, 101(C9), 20525-20542. https://doi.org/10.1029/96JC01849

Yasuda, I. (1997). The origin of the North Pacific intermediate water. Journal of Geophysical

Research: Oceans, 102(C1), 893-909. https://doi.org/10.1029/96JC02938
Yagi, M., Yasuda, I., Tanaka, T., Tanaka, Y., Ono, K., Ohshima, K. I., Katsumata, K. (2014). Re-evaluation of turbulent mixing vertical structure in the Bussol' Strait and its impact on water masses in the Okhotsk Sea and the North Pacific. Progress in Oceanography, 126, 121-134. https://doi.org/10.1016/j.pocean.2014.04.023

Figure Captions

Fig. 1: Bathymetry and observation sites. (a) Bathymetry with contours at 100 m and 200 m, and at 1000 m intervals for depths exceeding 1000 m. Thick lines indicate the 200 m and 2000 m contours. (b) Transects with bathymetry. The red line represents the EW line, blue for the S line, and green for the NS line. CTD sites are marked with crosses. Contour intervals are 25 m for depths shallower than 200 m (dashed lines) and 100 m (solid lines). Thick lines represent 500 m intervals.

Fig. 2: Vertical sections along the EW line. (a, d, g) Turbidity (color and black contours) and potential density (white contours), (b, e, h) potential temperature (color and black contours) and salinity (white contours), (c, f, i) ΔAOU/ΔS (color and black contours) and turbidity (white contours) observed in (a-c) December 2020, (d-f) April 2021, and (g-i) May 2022. Contour intervals are as follows: turbidity at 0.1 FTU, potential density at 0.1 σ_θ, potential temperature at 1 °C, salinity at 0.2 psu, ΔAOU/ΔS at 100 μmol/l/psu, and turbidity (white contours on the right) at 0.2 FTU. The horizontal axis represents the distance from the shore along the transect, with triangles below indicating measurement positions.

Fig. 3: Similar to Fig. 2, but for the S line (a-f) and the NS line (g-i). (a, d, g) Turbidity (color and black contours) and potential density (white contours), (b, e, h) potential temperature (color and black contours) and salinity (white contours), (c, f, i) ΔAOU/ΔS (color and black contours) and turbidity (white contours) observed in (a-c) December 2020, (d-f) April 2021, and (g-i) May 2022. Contour intervals are as follows: turbidity at 0.1 FTU (0.5 FTU in panel a), potential density at 0.1 σ_θ, potential temperature at 1 °C, salinity at 0.2 psu, ΔAOU/ΔS at 100 μmol/l/psu, and turbidity (white contours on the right) at 0.2 FTU (0.5 and 1 FTU in panel c). The horizontal axis represents the distance along the lines from the shore (a-f) and from the southernmost site (g-i), with triangles below indicating measurement positions.

Fig. 4: Scatter plots of salinity (psu) vs. (a, b) potential temperature (θ, °C), (c, d) apparent oxygen utilization (AOU, μmol/l), (e) ΔAOU/ΔS, and (f) Δθ, as well as turbidity (FTU) vs. (g)

ΔAOU/ΔS and (h) Δθ. Black, blue, and red colors in (a, c, e-h) correspond to data observed in December 2020, April 2021, and May 2022, respectively. Turbidity (FTU) is shown by color in (b, d). Solid circles and crosses indicate points in and outside the upper right region of the green lines in (a), respectively. The purple line in (a) is the fitting curve used to identify Soya Strait origin waters based on temperature. The green cross in (c) marks the reference point (S_o, AOU_o) for ΔAOU/ΔS. Data points exceeding the plot range are plotted on the corresponding axis. In (g, h), data points with fluorescence > 0.3 (flSP), AOU < 0, or S > 34.1 are excluded. The abbreviations in (a, c) are as follows: Soya Warm Current Water (SWCW), dense Soya Warm Current Water (dSWCW), Kuril Basin subsurface water (KBSSW), Dense Shelf Water (DSW), dichothermal water (DTW), East Sakhalin Current Water (ESCW), Kuril Basin surface water (KBSW). For details of water mass definitions, refer to Takizawa (1982) and a review by Mundo et al. (2024).

Fig. 5: Horizontal distributions of (a, c, e, g) bottom mixed-layer thickness (m) and (b, d, f, h) potential density (σ_θ, contours) and bottom mixed-layer thickness (color) in (a, b) spring (Apr–Jun), (c, d) summer (Jul–Sep), (e, f) autumn (Oct–Dec), and (g, h) winter (Jan–Mar), estimated from past observation data (HRO and JODC). Contour intervals are 20 m on the left and 0.2 σ_θ on the right. Red lines represent monthly mean bottom streamlines from the JPN system for May, August, November, and February. The onshore side of these streamlines marks the main pathway of Soya Strait origin waters. Dashed lines indicate the 300 m isobath, with analyses confined to shallower areas. Black dots indicate observation locations.

Fig. 6: Monthly means of (a, d, g) bottom mixed-layer thickness (m, color) with bottom streamline, (b, e, h) bottom potential density (σ_θ), and (c, f, i) bottom salinity (psu, color) with potential temperature (°C) in (a-c) January, (d-f) May, (g-i) August. Temperature contour interval is 2°C. Data are 10-year monthly means from the JPN system for the shelf area (shallower than 330 m) from 2008 to 2017. The square in (a) represents the region of area average in Fig. 7.

Fig. 7: Seasonal variations of (left axis) bottom mixed-layer thickness (m, red) and (right axes) potential density (σ_θ, green), potential temperature (°C, blue), and salinity (psu, black) at the bottom. The values are monthly means for the period 2008–2017 of the area average over the square region in Fig. 6a (44.25–44.39°N, 144–144.3°E), from the JPN system.

Fig. 8: Monthly means of (a, d, g) log10 of vertical diffusivity coefficient at 15 m above the bottom (cm^2/s), (b, e, h) bottom flow speed (cm/s), and (c, f, i) tendency of vertical density stratification changes due to horizontal density advection (r.h.s of Eq. (3); 10^{-5} s^{-1}) in (a-c) January, (d-f) May, (g-i) August. As in Fig. 6, data are 10-year monthly means from the JPN system for the shelf area (shallower than 330 m) from 2008 to 2017.

Fig. 9: Distribution of particle passage frequency for one year, categorized by initial densities: (a) $\sigma_\theta < 26.0$, (b) $26.0 \leq \sigma_\theta < 26.7$, and (c) $\sigma_\theta \geq 26.7$. (d) Horizontal region where particles were initially placed within the bottom mixed layer, and tracked for one year from August 1, 2012. The unit is number of passages/(year · horizontal grid).

Fig. 10: Distribution of monthly particle passage frequency after (a, d, g) one, (b, e, h) three, and (c, f, i) five months from the start of tracking, categorized by initial densities: (a-c) $\sigma_\theta < 26.0$, (d-f) $26.0 \leq \sigma_\theta < 26.7$, and (g-i) $\sigma_\theta \geq 26.7$. As in Fig. 9, particles within the bottom mixed layer on the Hokkaido shelf were tracked from August 1, 2012. The unit is number of passages/(month · horizontal grid).

Fig. 11: Time evolution of the number of tracked particles in the (gray line) Okhotsk Sea and (red line) North Pacific, categorized by initial densities: (a, d, g) $\sigma_\theta < 26.0$, (b, e, h) $26.0 \leq \sigma_\theta < 26.7$, and (c, f, i) $\sigma_\theta \geq 26.7$. The unit is percentage to the initial particle number in each density range. Cases with (a-c) no sinking velocity as in Figs. 9 and 10 and sinking velocity of (d-f) 0.4 m/day and (g-i) 4 m/day. As in Fig. 9, particles within the bottom mixed layer on the Hokkaido shelf were tracked from August 1, 2012.

Fig. 12: Seasonal variations in the annual particle passage frequency, including all density ranges. Tracking started on the 1st of (a) January, (b) May, and (c) August 2012. The unit is number of passages/(year · horizontal grid).

Fig. 13: Seasonal variations in the timescale for particles to enter the North Pacific. (a) Outflow ratio: percentage of particles in the North Pacific after one year of tracking. (b) Number of days until 50% of tracked particles entered the North Pacific. Particles are categorized by initial densities: (blue) $\sigma_\theta < 26.0$, (orange) $26.0 \leq \sigma_\theta < 26.7$, and (gray) $\sigma_\theta \geq 26.7$. Months are not plotted, if tracked particles were fewer than 200 (April–June for $\sigma_\theta < 26.0$, November to January for $\sigma_\theta \geq 26.7$), or if 50% did not exit within one year with sufficient particle numbers (March–June for $26.0 \leq \sigma_\theta < 26.7$, March-October for $\sigma_\theta \geq 26.7$).

Fig. 14: Annual particle passage frequency for years 2008–2016. Particles within the bottom mixed layer on the Hokkaido shelf were tracked on the 26.6 σ_θ surface from August 1st in each year. Values on the color scale should be doubled for 2012. The unit is number of passages/(year · horizontal grid).

Fig. 15: Interannual variability in the outflow ratio (percentage of particles in the North Pacific) after one year, calculated for 2008 to 2016 on the 26.6 σ_θ surface.

Fig. A1: Monthly means of flow speed (cm/s) and streamline at 50 m depth in (a) January, (b) May, and (c) August, averaged from 2008 to 2017.

Fig. A2: Scatter plots of salinity (psu) vs. potential temperature (°C) in (a) January (purple), May (red), and August (green) and in (b) April (blue), May (red), and December (black). Data plotted are at 47°N from the coast to 146°E and are daily means on day 15 of the corresponding months from 2008 to 2017.

Fig. B1: Scatter plots of (a) potential temperature (θ, °C), (b) apparent oxygen utilization (AOU, μmol/l), (c) dissolved oxygen (O, μmol/l), (d) oxygen saturation (S_{O2}, %), (e) $-\Delta O/\Delta S$, and (f) $-\Delta S_{O2}/\Delta S$ vs. salinity (psu), and (g) $-\Delta O/\Delta S$ and (h) $-\Delta S_{O2}$ vs. turbidity (FTU). Black, blue, and red colors correspond to observations from December 2020, April 2021, and May 2022, respectively. Solid circles and crosses indicate points in and outside the upper right region of the green lines in (a), respectively. Green crosses in (b-d) mark reference points for $\Delta AOU/\Delta S$, $-\Delta O/\Delta S$, and $-\Delta S_{O2}/\Delta S$. Data exceeding the plot range are plotted on the corresponding axis. In (g, h), points with fluorescence > 0.3 (flSP), AOU < 0, or S > 34.1 are excluded.

Fig. C1: Estimation of bottom mixed-layer thickness. The bottom mixed-layer thickness was defined as $D_b - D_u$, where D_b is the bottom depth, and D_u is the depth of the upper boundary of the bottom mixed layer. To determine D_u, D_i and Do were used, where D_i is the depth of the lower boundary of the interior, defined as the observed layer where the difference in potential density from the deepest layer observed (D_o) first exceeded a threshold ($\Delta\sigma_\theta$ set to 0.125).

Fig. C2: Scatter plot of estimated mixed-layer thickness ($D_b{-}D_u$) vs. the difference between bottom depth and the depth of the deepest layer observed ($D_b{-}D_o$), using HRO and JODC data.

Table List

Table 1: Summary of observation cruises.

Table C1: Number of JODC and HRO data in the analysis region: Numbers of observation sites, observed layers, observation sites without measured depths, sites where the bottom depth was shallower than the deepest layer observed ($D_b < D_o$), sites deeper than 300 m ($D_b > 300$ m), sites with a depth difference between the bottom and deepest layer observed ($D_b{-}D_o$) greater than 50 m, and sites used for analysis. For observation sites without measured bottom depth and sites where $D_b < D_o$, the bottom depth was estimated using existing bathymetric data.

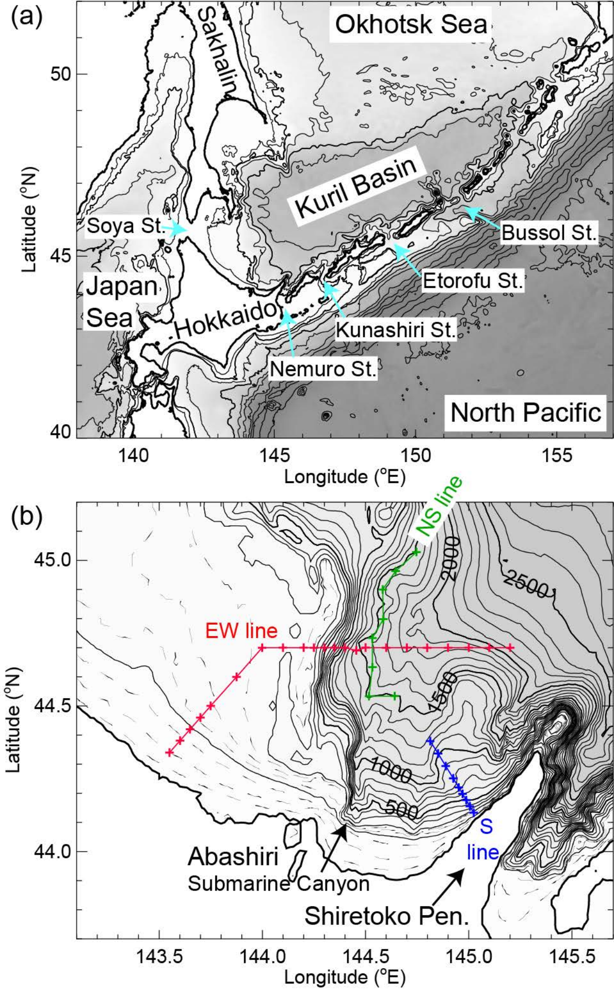
(a)
Okhotsk Sea
Sakhalin
Kuril Basin
Soya St.
Bussol St.
Etorofu St.
Japan Sea
Hokkaido
Kunashiri St.
Nemuro St.
North Pacific
Latitude (°N)
Longitude (°E)
(b)
NS line
2000
2500
EW line
1500
1000
500
S line
Abashiri
Submarine Canyon
Shiretoko Pen.
Latitude (°N)
Longitude (°E)

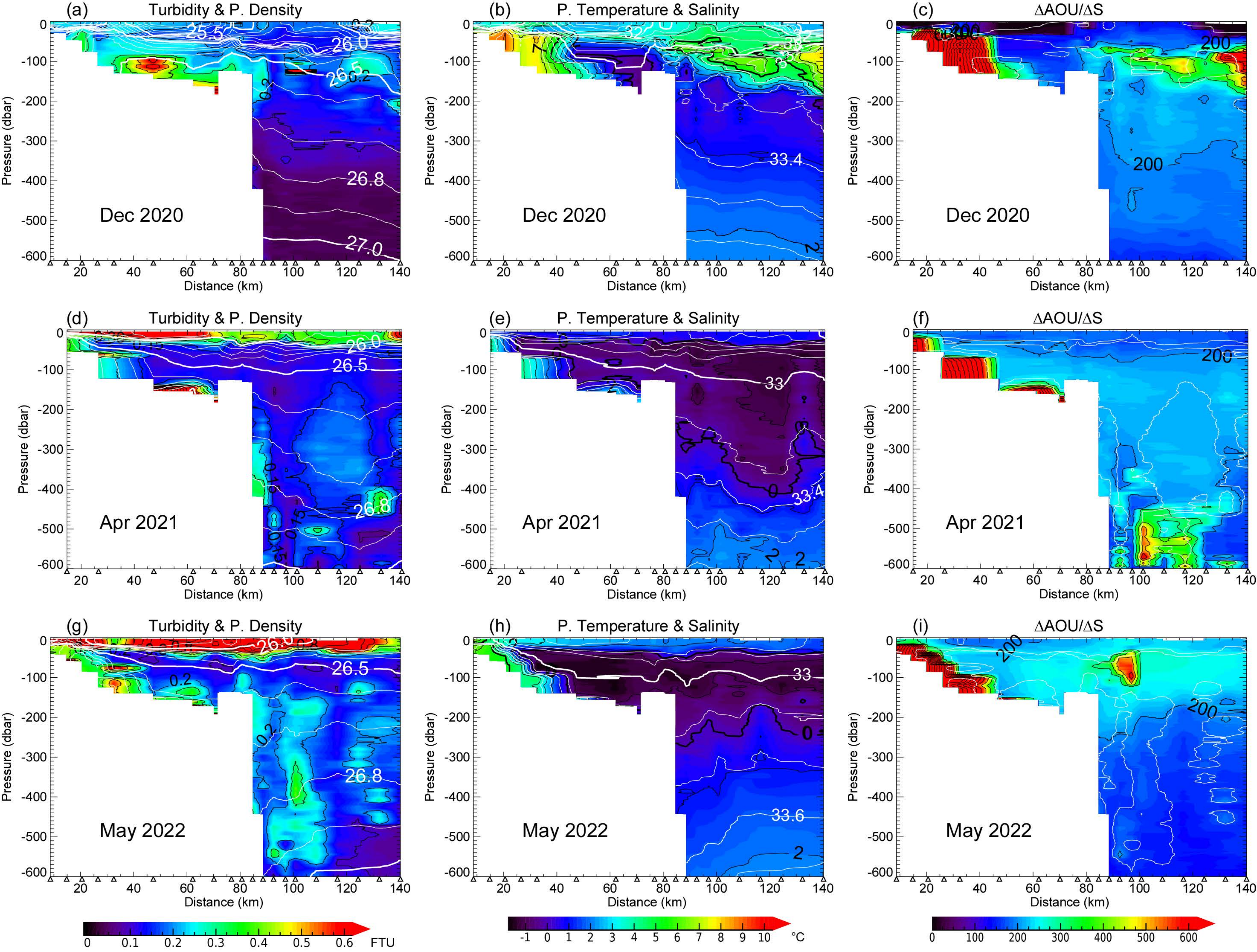

(a) Turbidity & P. Density
(b) P. Temperature & Salinity
(c) ΔAOU/ΔS
(d) Turbidity & P. Density
(e) P. Temperature & Salinity
(f) ΔAOU/ΔS
(g) Turbidity & P. Density
(h) P. Temperature & Salinity
(i) ΔAOU/ΔS
Dec 2020
Apr 2021
May 2022
Pressure (dbar)
Distance (km)
FTU
°C

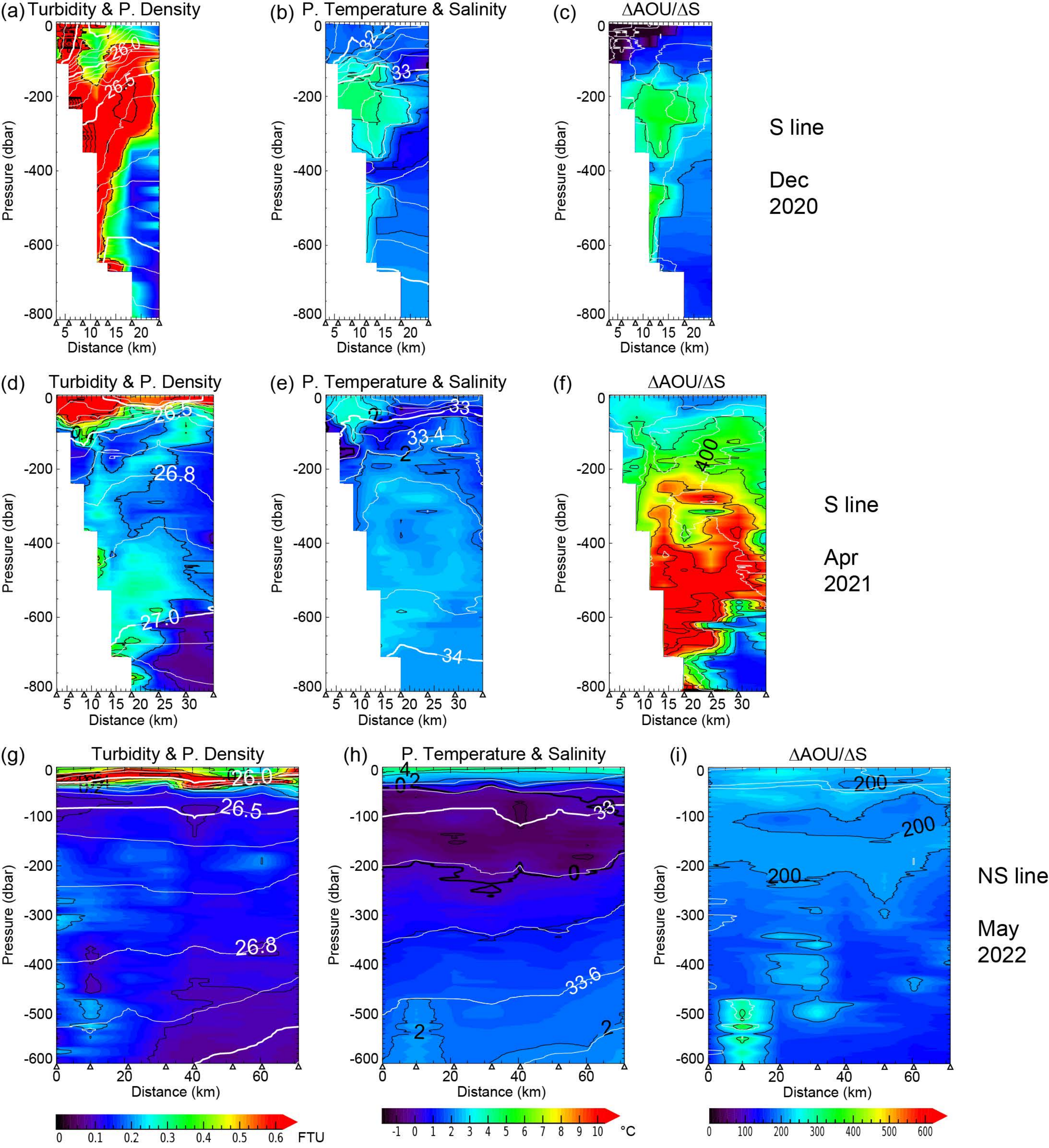

(a) Turbidity & P. Density
(b) P. Temperature & Salinity
(c) ΔAOU/ΔS
S line
Dec 2020
(d) Turbidity & P. Density
(e) P. Temperature & Salinity
(f) ΔAOU/ΔS
S line
Apr 2021
(g) Turbidity & P. Density
(h) P. Temperature & Salinity
(i) ΔAOU/ΔS
NS line
May 2022
Pressure (dbar)
Distance (km)
FTU
°C

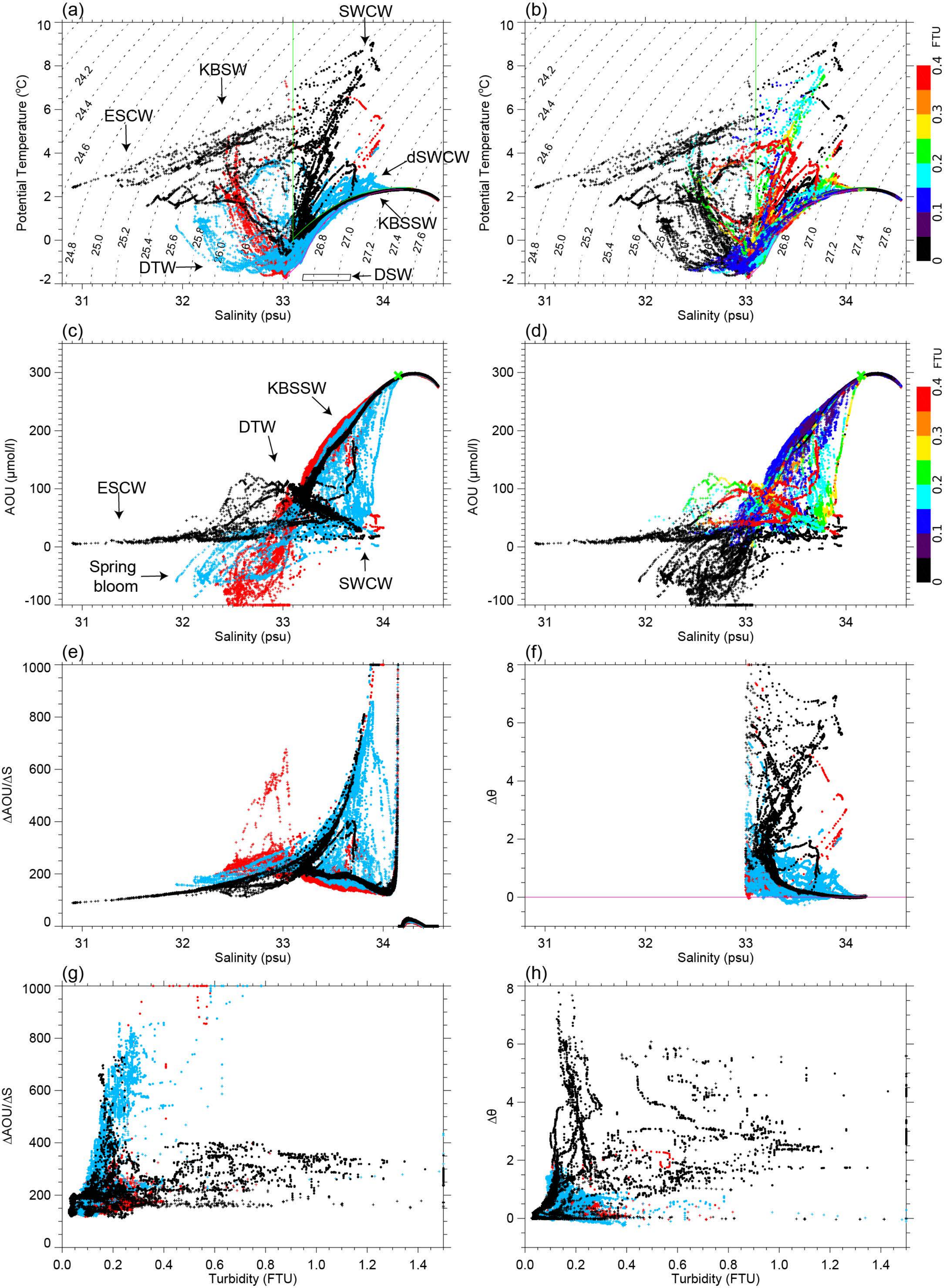

(a)
(b)
(c)
(d)
(e)
(f)
(g)
(h)
SWCW
KBSW
ESCW
dSWCW
KBSSW
DTW
DSW
Spring bloom
Potential Temperature (°C)
Salinity (psu)
AOU (µmol/l)
ΔAOU/ΔS
Δθ
Turbidity (FTU)
FTU

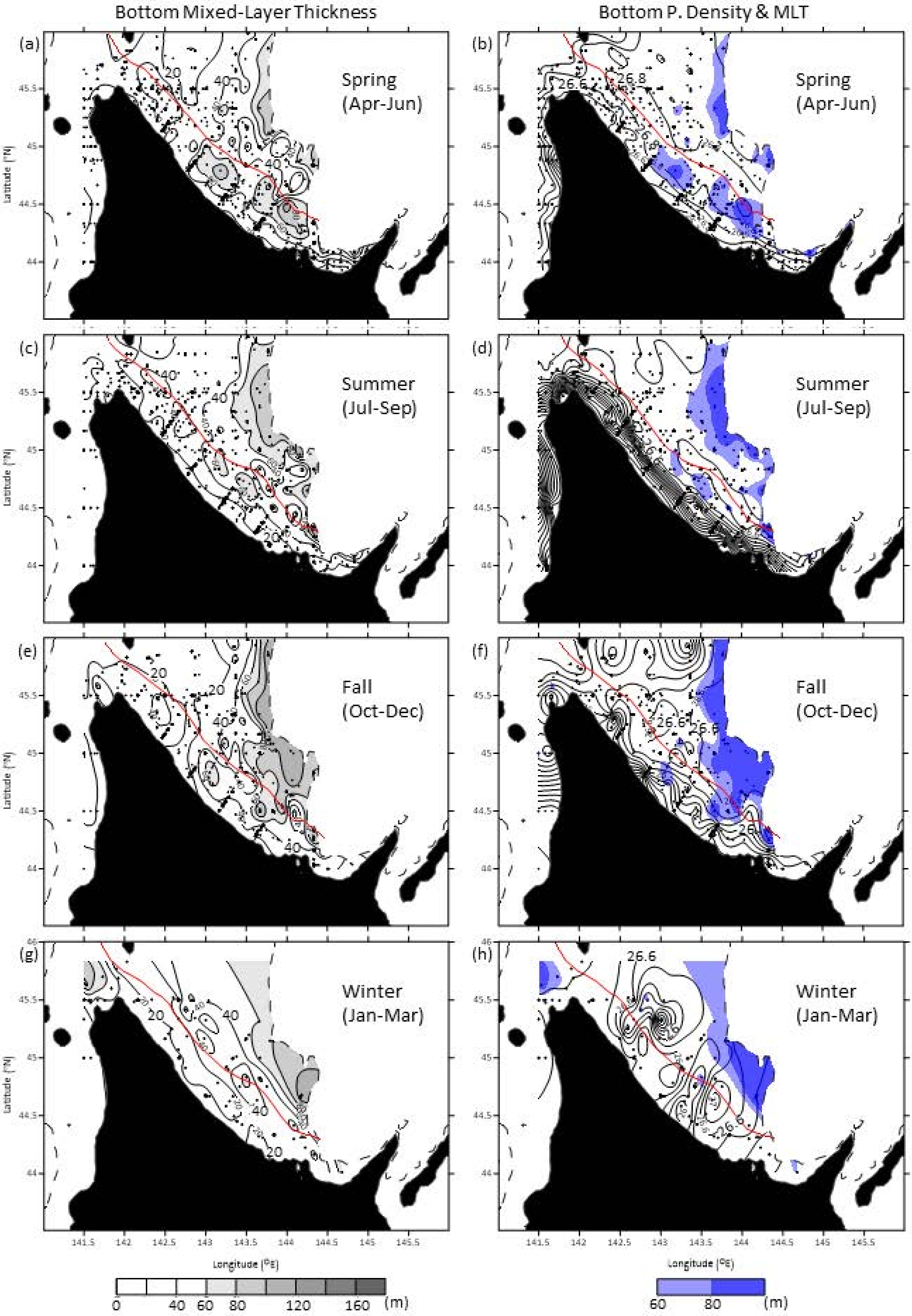

Bottom Mixed-Layer Thickness
Bottom P. Density & MLT
(a)
Spring
(Apr-Jun)
(b)
Spring
(Apr-Jun)
(c)
Summer
(Jul-Sep)
(d)
Summer
(Jul-Sep)
(e)
Fall
(Oct-Dec)
(f)
Fall
(Oct-Dec)
(g)
Winter
(Jan-Mar)
(h)
Winter
(Jan-Mar)
Latitude (°N)
Longitude (°E)
0
40
60
80
120
160
(m)
60
80
(m)

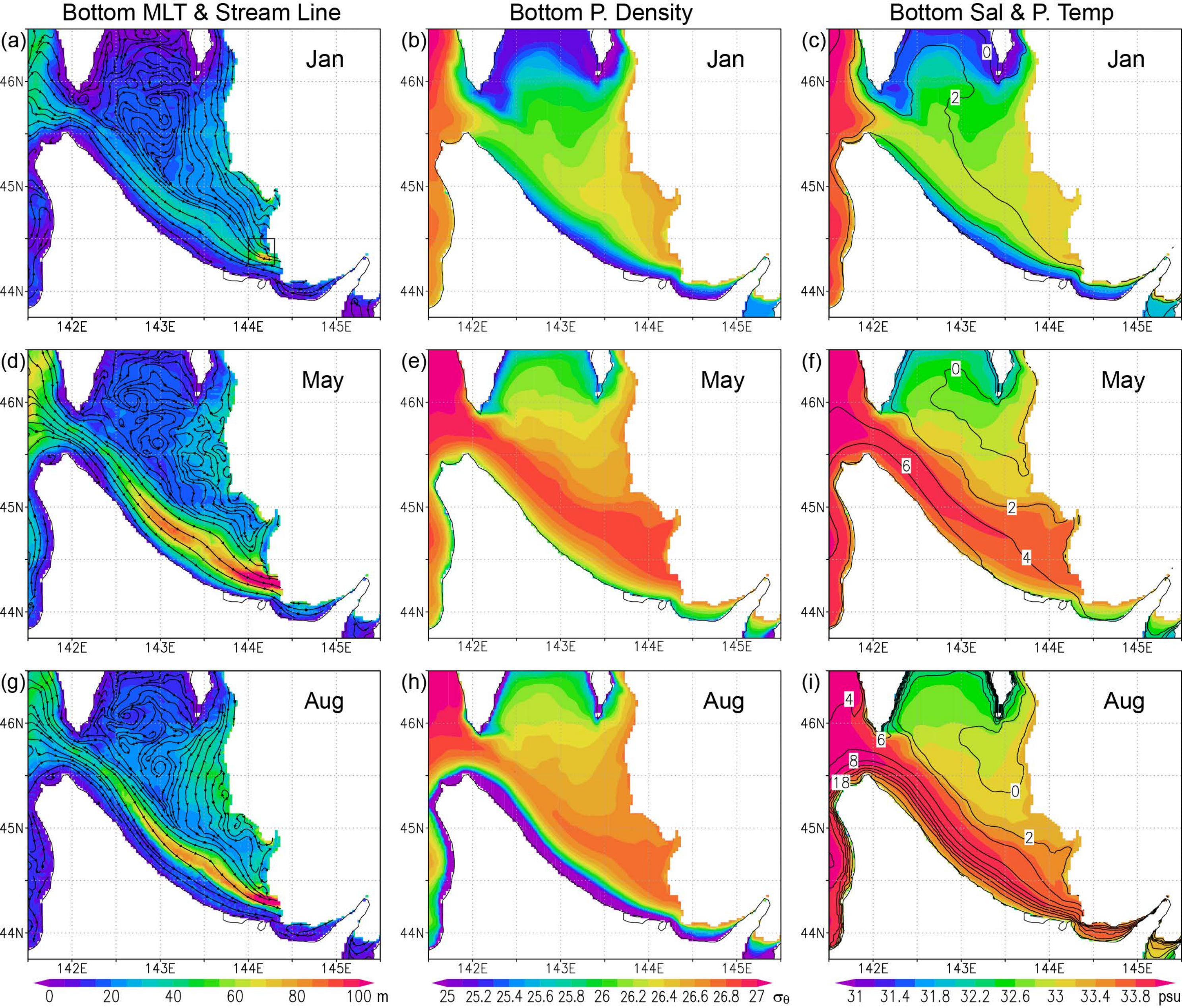

Bottom MLT & Stream Line
Bottom P. Density
Bottom Sal & P. Temp
(a)
Jan
(b)
Jan
(c)
Jan
(d)
May
(e)
May
(f)
May
(g)
Aug
(h)
Aug
(i)
Aug
46N
45N
44N
142E
143E
144E
145E
0
2
6
4
8
18
0 20 40 60 80 100 m
25 25.2 25.4 25.6 25.8 26 26.2 26.4 26.6 26.8 27 σθ
31 31.4 31.8 32.2 32.6 33 33.4 33.8 psu

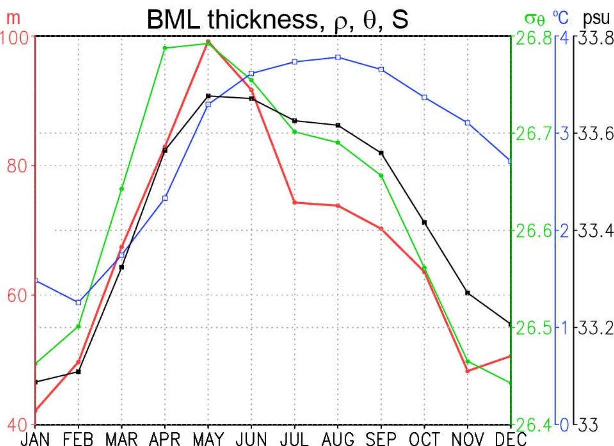

BML thickness, ρ, θ, S
m
σθ
ºC
psu
100
80
60
40
26.8
26.7
26.6
26.5
26.4
4
3
2
1
0
33.8
33.6
33.4
33.2
33
JAN
FEB
MAR
APR
MAY
JUN
JUL
AUG
SEP
OCT
NOV
DEC

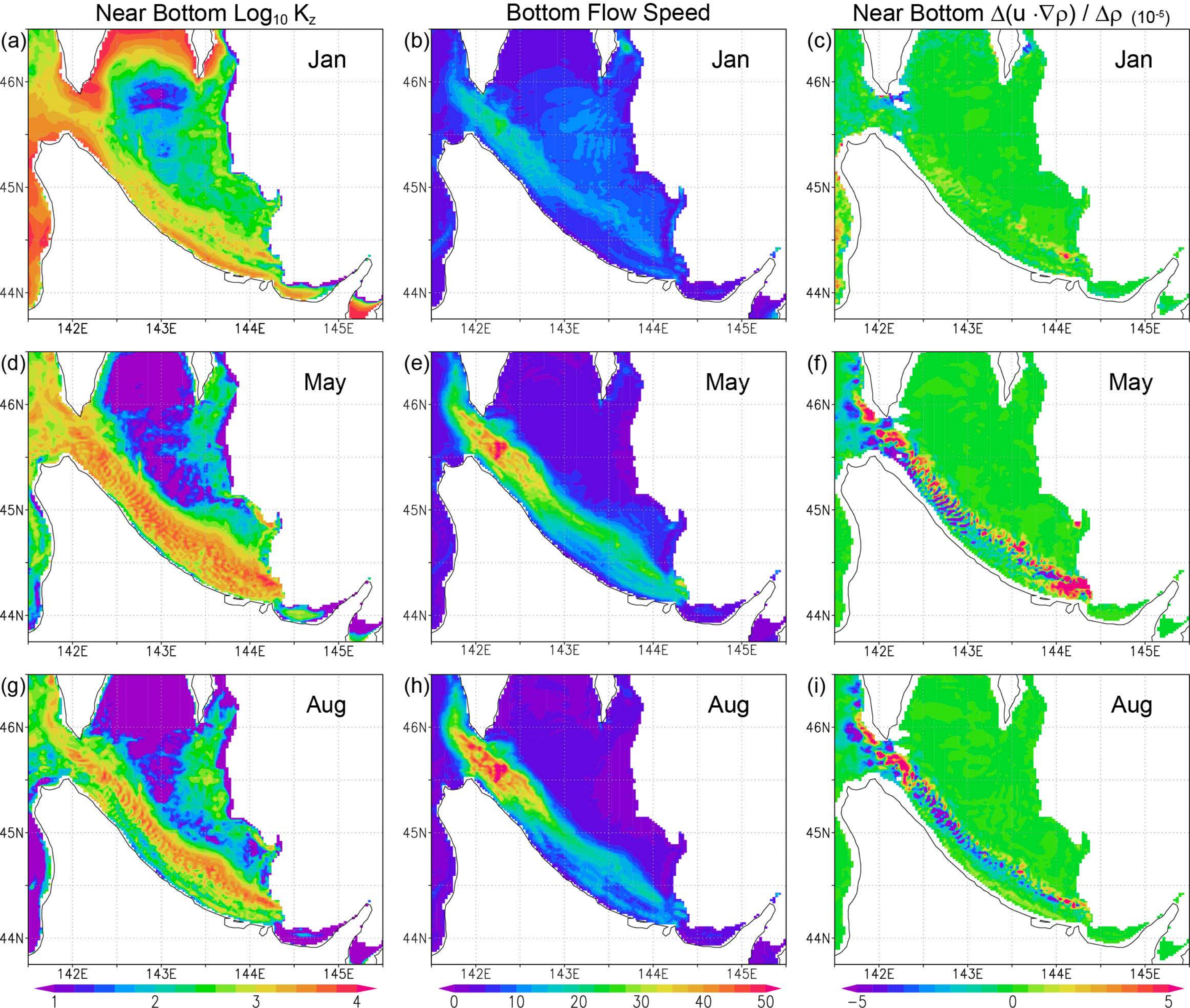

Near Bottom $Log_{10} K_z$
Bottom Flow Speed
Near Bottom $\Delta(u \cdot \nabla\rho) / \Delta\rho$ (10^{-5})
(a)
Jan
(b)
Jan
(c)
Jan
(d)
May
(e)
May
(f)
May
(g)
Aug
(h)
Aug
(i)
Aug
46N
45N
44N
142E
143E
144E
145E
1
2
3
4
0
10
20
30
40
50
−5
0
5

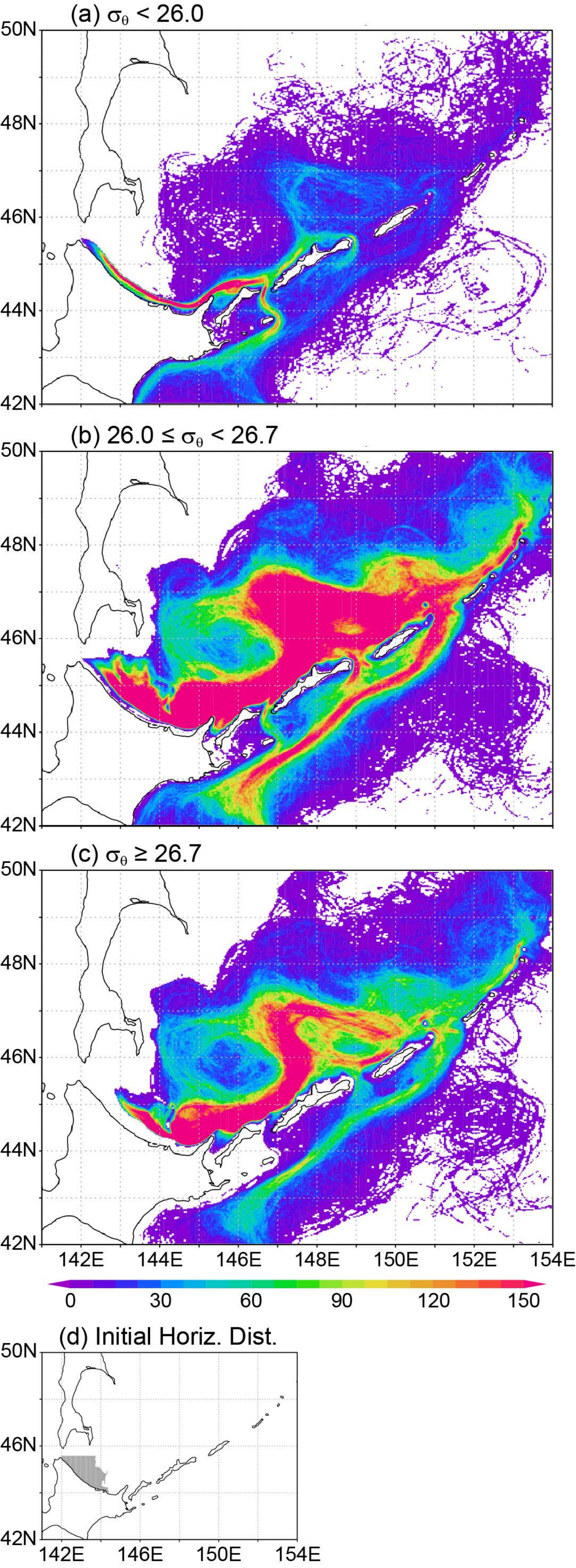

(a) σ_θ < 26.0
(b) 26.0 ≤ σ_θ < 26.7
(c) σ_θ ≥ 26.7
(d) Initial Horiz. Dist.
50N
48N
46N
44N
42N
142E
144E
146E
148E
150E
152E
154E
0
30
60
90
120
150

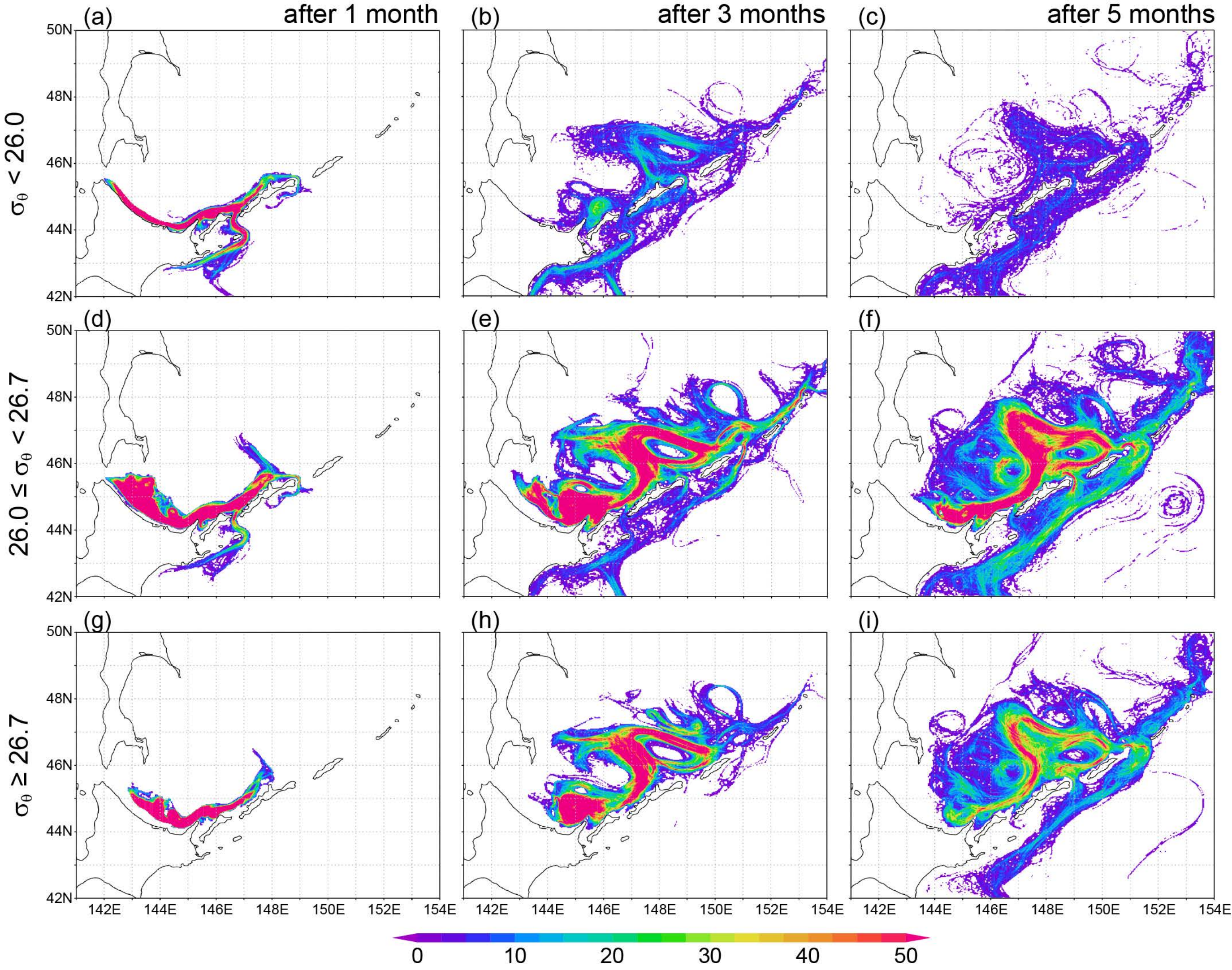

(a)
after 1 month
(b)
after 3 months
(c)
after 5 months
(d)
(e)
(f)
(g)
(h)
(i)
$\sigma_\theta < 26.0$
$26.0 \leq \sigma_\theta < 26.7$
$\sigma_\theta \geq 26.7$
50N
48N
46N
44N
42N
142E
144E
146E
148E
150E
152E
154E
0
10
20
30
40
50

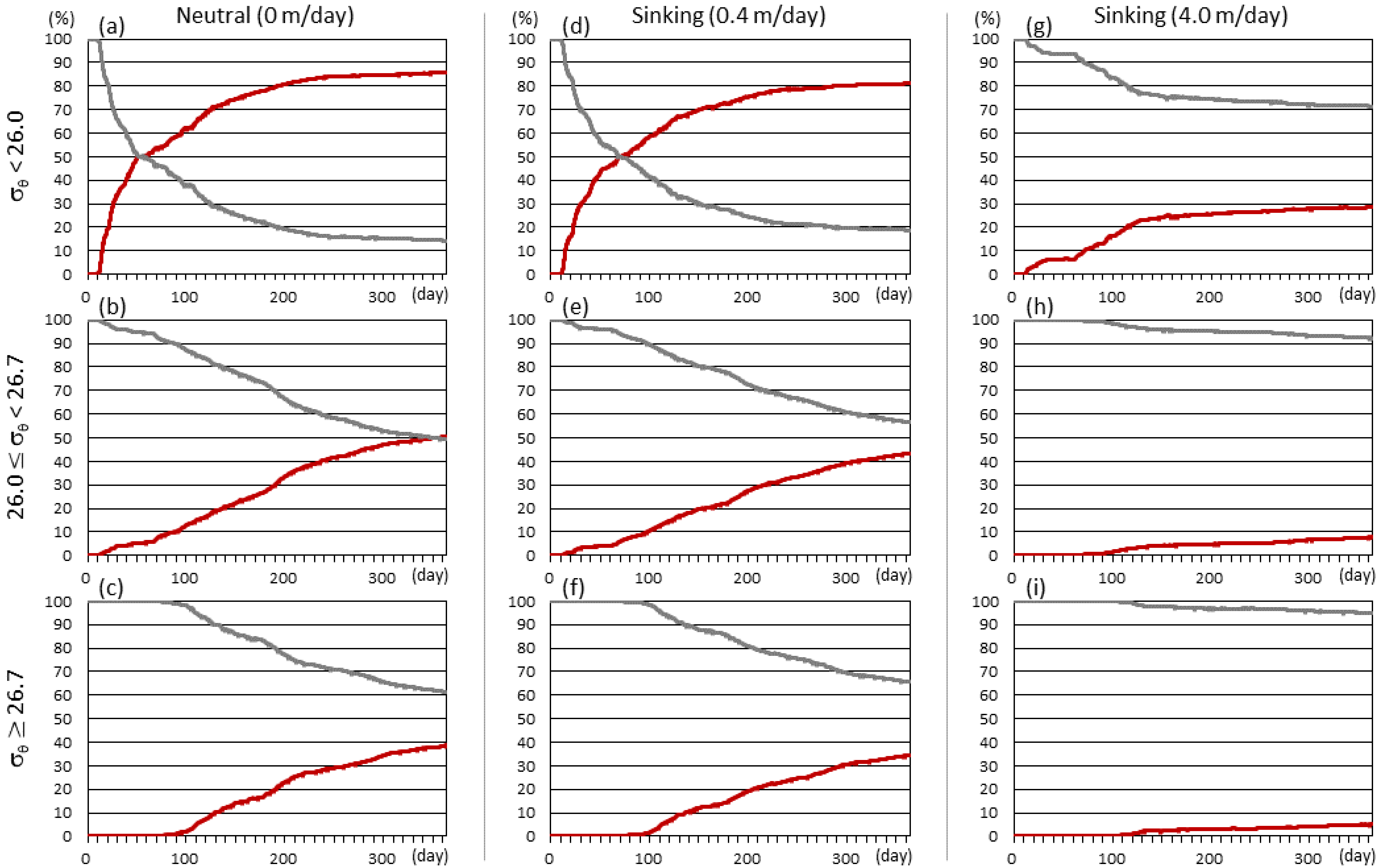

Neutral (0 m/day)
Sinking (0.4 m/day)
Sinking (4.0 m/day)
(a)
(b)
(c)
(d)
(e)
(f)
(g)
(h)
(i)
$\sigma_\theta < 26.0$
$26.0 \leq \sigma_\theta < 26.7$
$\sigma_\theta \geq 26.7$
(%)
(day)

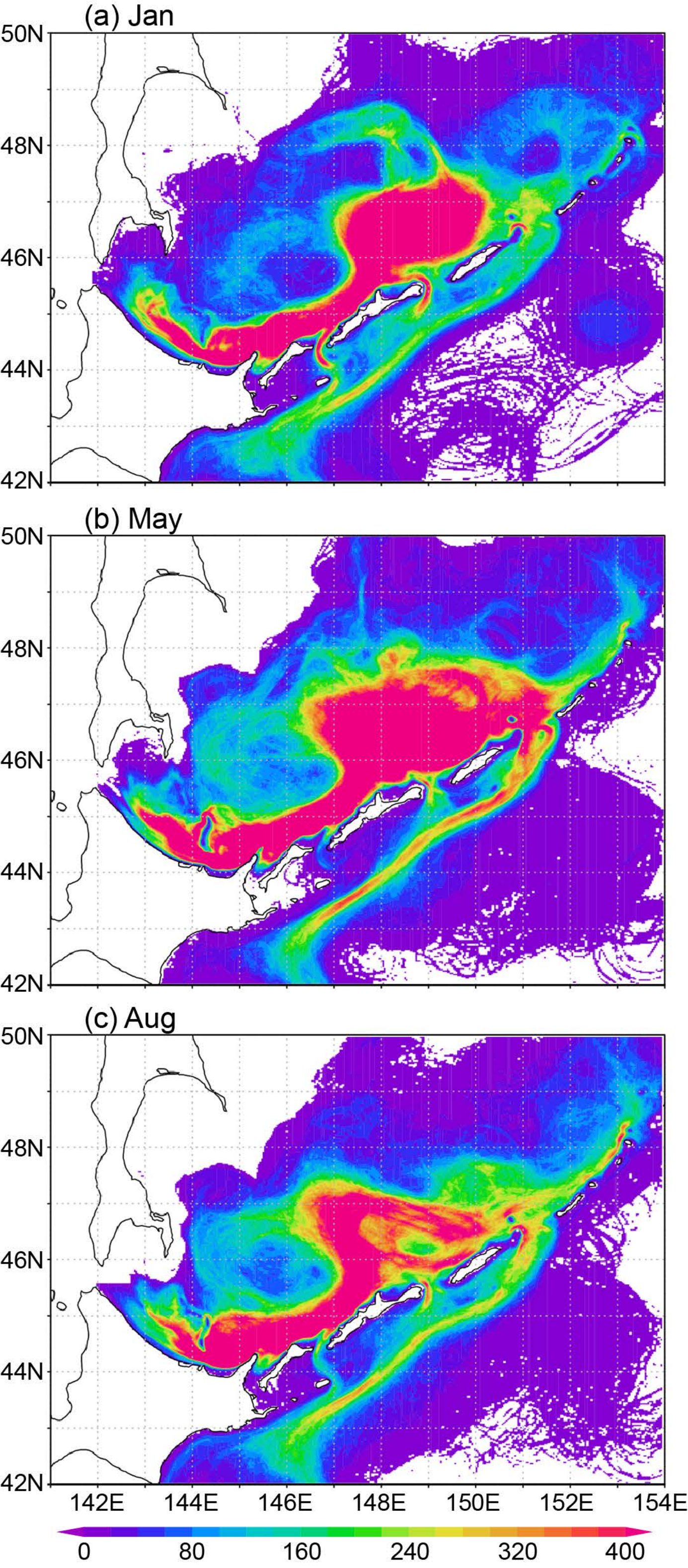
(a) Jan
(b) May
(c) Aug
50N
48N
46N
44N
42N
142E
144E
146E
148E
150E
152E
154E
0
80
160
240
320
400

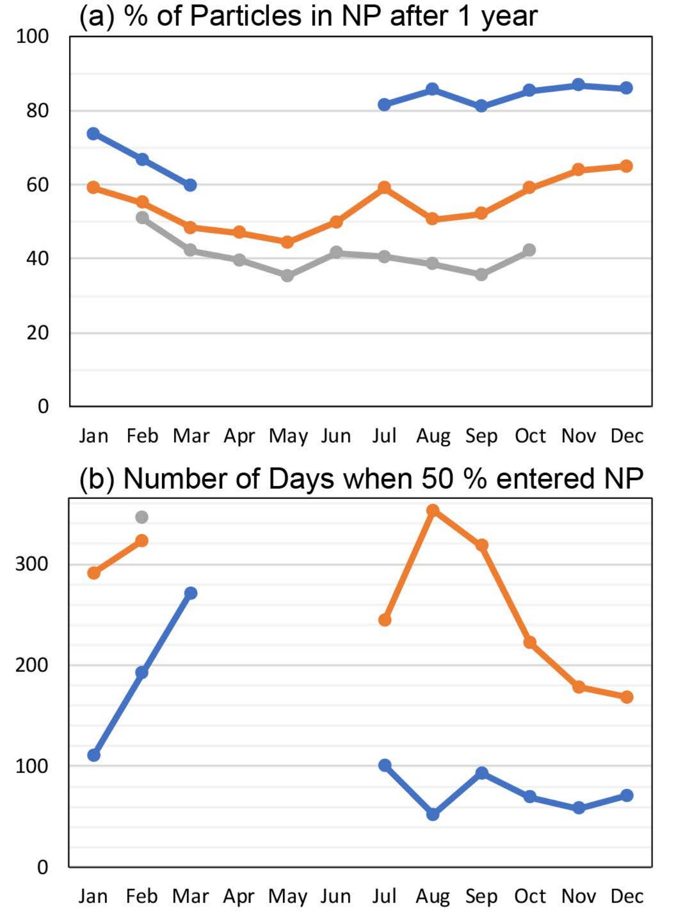
(a) % of Particles in NP after 1 year
100
80
60
40
20
0
Jan Feb Mar Apr May Jun Jul Aug Sep Oct Nov Dec
(b) Number of Days when 50 % entered NP
300
200
100
0
Jan Feb Mar Apr May Jun Jul Aug Sep Oct Nov Dec

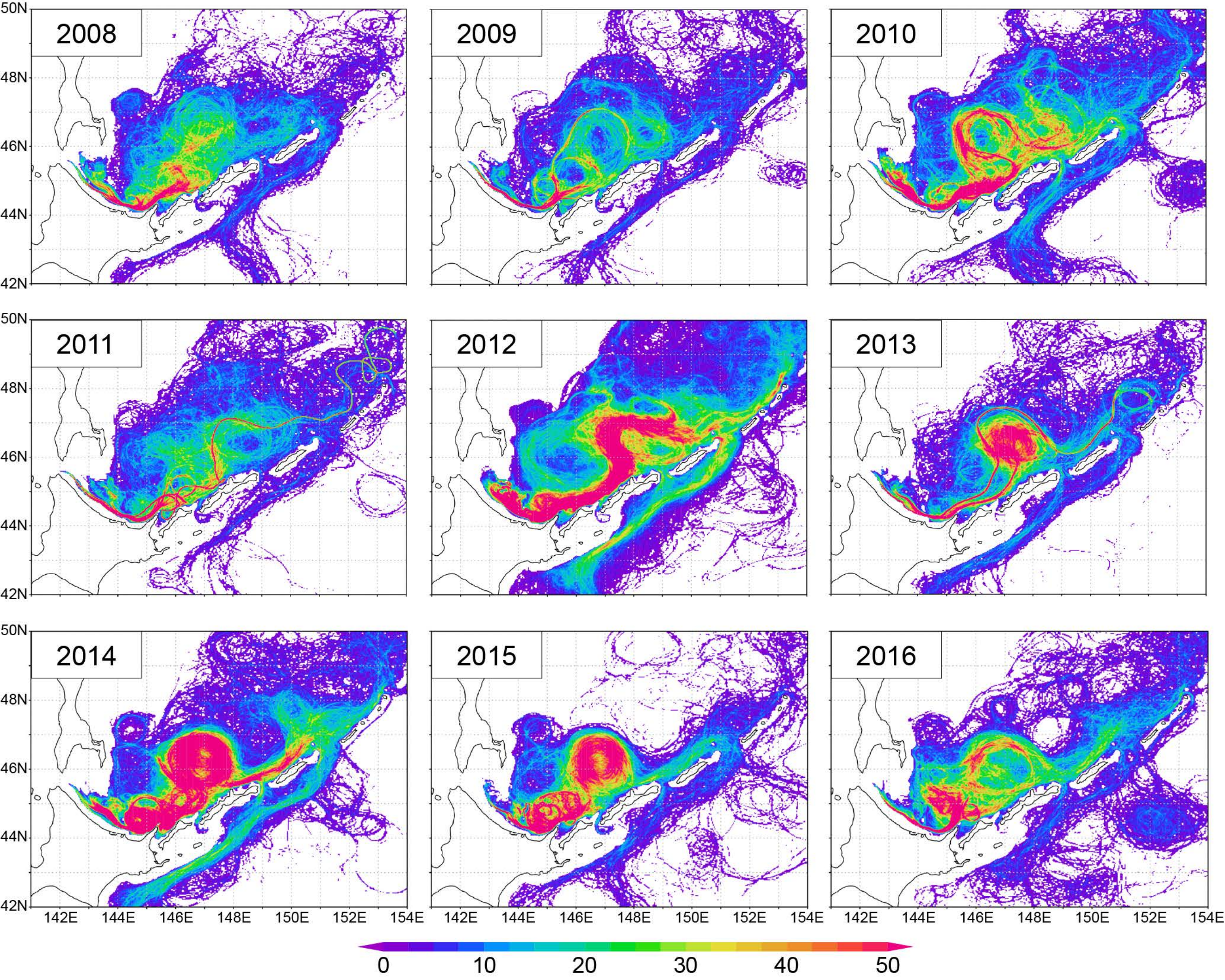

2008
2009
2010
2011
2012
2013
2014
2015
2016
50N
48N
46N
44N
42N
142E
144E
146E
148E
150E
152E
154E
0
10
20
30
40
50

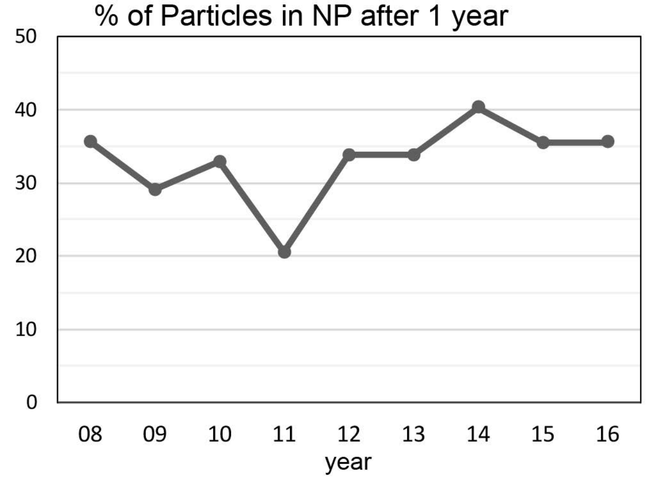
% of Particles in NP after 1 year
50
40
30
20
10
0
08
09
10
11
12
13
14
15
16
year

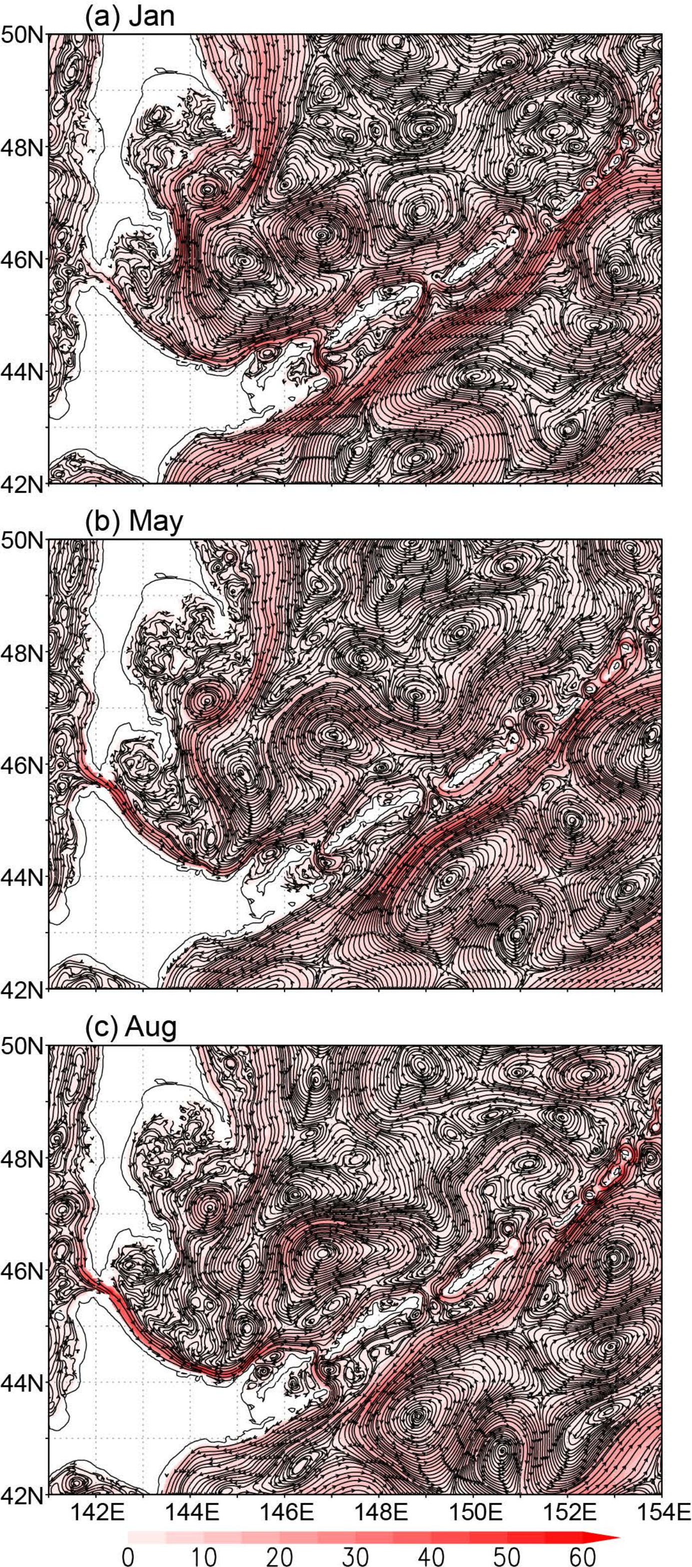
(a) Jan
(b) May
(c) Aug
50N
48N
46N
44N
42N
142E
144E
146E
148E
150E
152E
154E
0
10
20
30
40
50
60

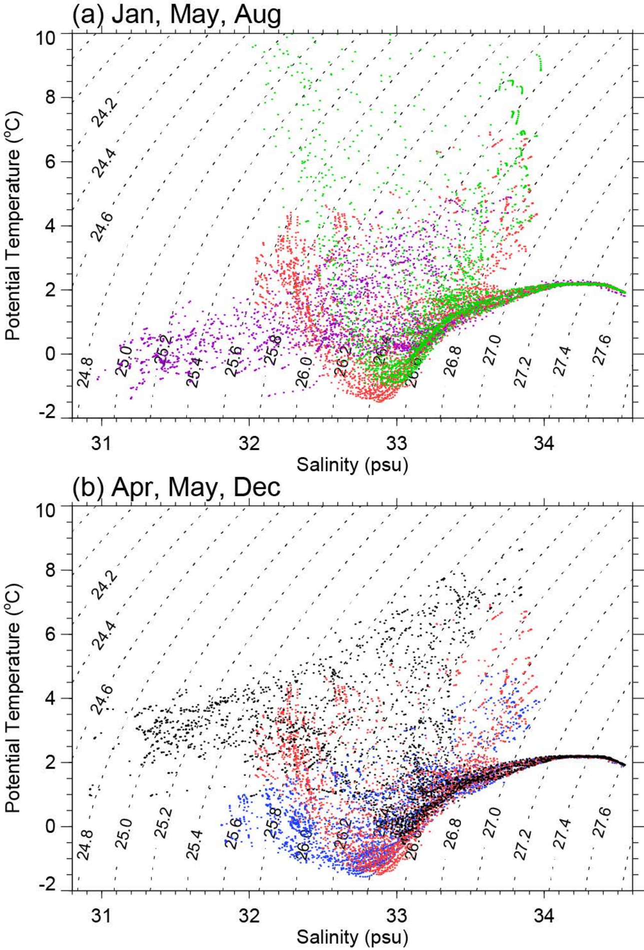
(a) Jan, May, Aug
Potential Temperature (°C)
Salinity (psu)
(b) Apr, May, Dec
Potential Temperature (°C)
Salinity (psu)
24.2
24.4
24.6
24.8
25.0
25.2
25.4
25.6
25.8
26.0
26.2
26.4
26.8
27.0
27.2
27.4
27.6

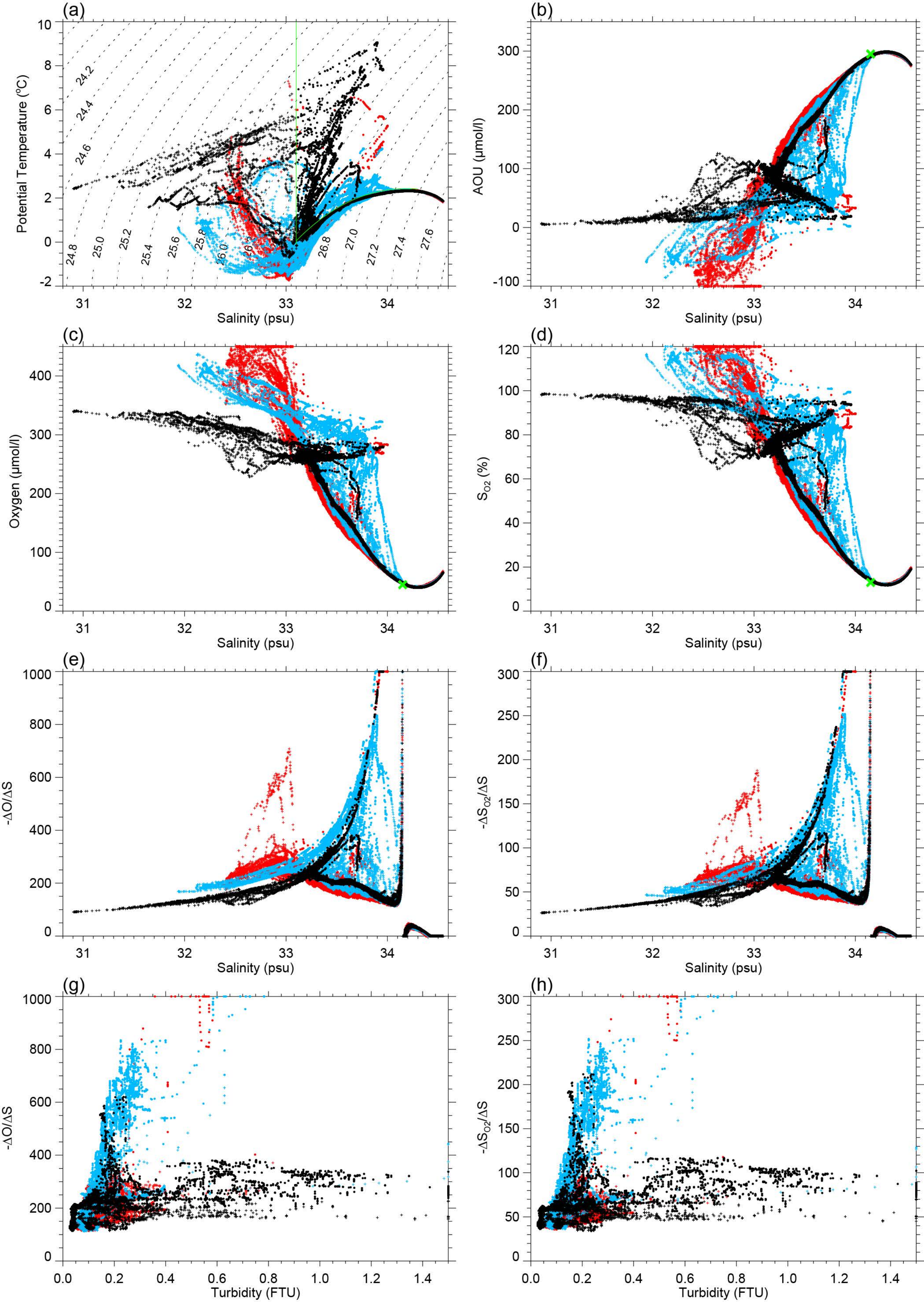

(a)
(b)
(c)
(d)
(e)
(f)
(g)
(h)
Potential Temperature (°C)
AOU (µmol/l)
Oxygen (µmol/l)
S_{O2} (%)
-ΔO/ΔS
$-\Delta S_{O2}/\Delta S$
Salinity (psu)
Turbidity (FTU)
24.2
24.4
24.6
24.8
25.0
25.2
25.4
25.6
25.8
26.0
26.8
27.0
27.2
27.4
27.6

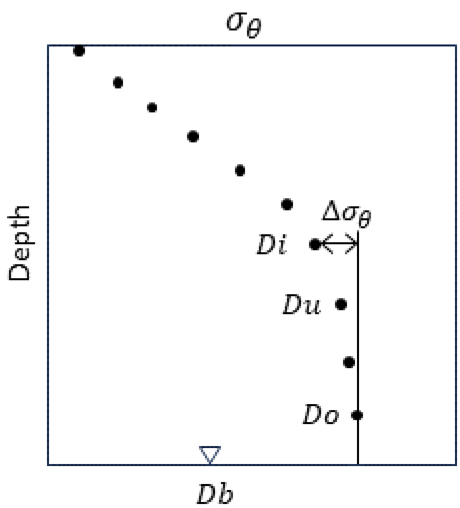

σ_θ
Depth
$\Delta\sigma_\theta$
Di
Du
Do
Db

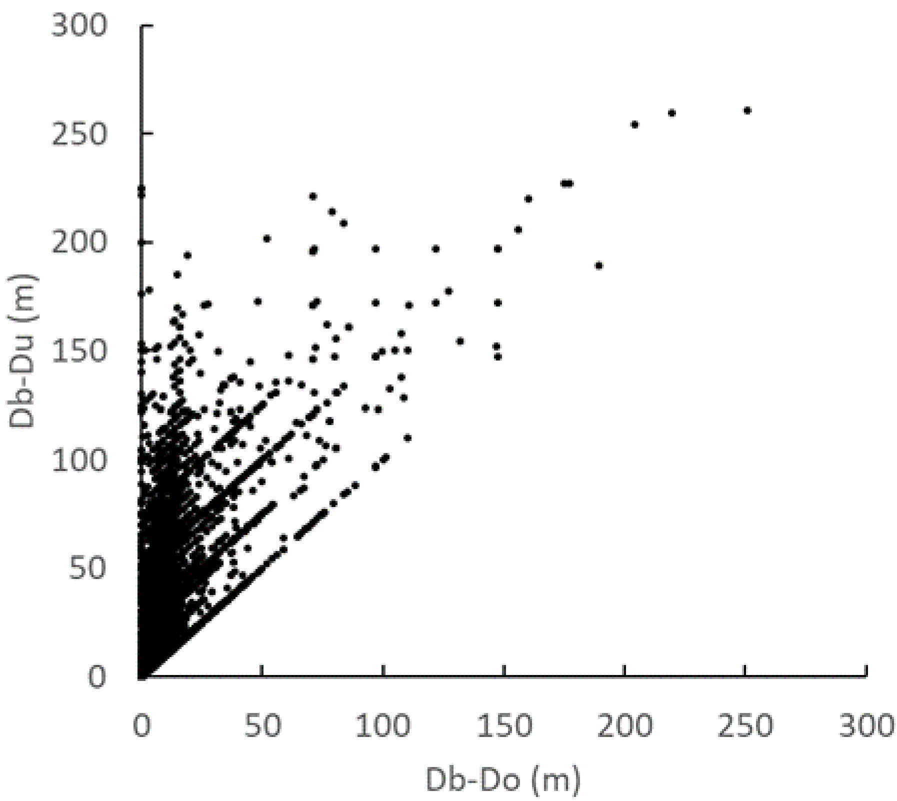

Db-Du (m)
Db-Do (m)
0
50
100
150
200
250
300

Cruise	Ship	Year, Mon.	Day	Transects
KH-20-12	Hakuho-Maru	2020, Dec.	12-14 21	EW line S line
KS-21-06	Shinsei-Maru	2021, Apr.	15-19, 23 18-19	EW line S line
KS-22-06	Shinsei-Maru	2022, May	1-5 12	EW line NS line

	sites	layers	no water -depth	Db < Do	Db > 300 m	Db-Do > 50 m	analyzed
JODC	4441	102057	4441	–	480	15	3946
HRO	3519	71438	197	109	791	134	2594